

UNIVERSITÀ DEGLI STUDI DI GENOVA
SCUOLA POLITECNICA



MASTER OF SCIENCE THESIS
IN
MECHANICAL ENGINEERING

**An Experimental and Numerical Investigation
on the Propagation of Compositional Waves**

Supervisor:

Prof. Alessandro Bottaro

Co-Supervisor:

Prof. Simone Hochgreb

Candidate:

Andrea Busseti

March 2018

I would like to dedicate this work to my loving parents, Roberta and Gian Luca, who have always been close to me during these months away from home. From them, as well as from Luca and Maddalena, I have always had valuable advice and support during difficult times. An equally big thank you goes to my girlfriend Ilaria, for having shared with me every day of this adventure. Thanks also to my loving grandmother Gianna, and a last thought to my grandparents Luciano, Vittorio, Consilia and “grandma” Ambra, that I hope would have been proud of me.

“Look up at the stars and not down at your feet. Try to make sense of what you see, and wonder about what makes the universe exist. Be curious.”

— Stephen Hawking

Acknowledgements

I would first like to thank my Supervisor, Professor Alessandro Bottaro, for giving me the opportunity of living a great study period abroad and for his support with every aspect of my work. An equally important thanks goes to Professor Simone Hochgreb, for having accepted me as an Academic Visitor under her guidance at the University of Cambridge. The opportunity she has given me is priceless, and I will always be thankful for this.

I acknowledge the PhD students F. De Domenico, J. Rodrigues and E. O. Rolland, for their precious help and valuable comments during my period of work as part of their group. I would also like to give a special thanks to my colleagues at the Hopkinson Lab in Cambridge, the Professors and Researchers I have been in contact with, the entire office staff and the technicians. A particular thought goes to my friends Dante, Hassan and Andrej, with which I spent great time also out of the office.

Finally, sincere thanks also to all the other people who made my stay in Cambridge the greatest experience of my life: the Erasmus students Andrea, Simon, Elena and Caroline, and my housemates Danny, Ciara, Andrew and Bahavin. I wish the best for all of them.

Abstract

Compositional inhomogeneities in accelerated gaseous flows have been recently proved to be a source of indirect noise, which may potentially contribute to the generation of thermoacoustic instabilities in gas-turbines combustors. Experiments carried out at the University of Cambridge on non-reacting ducted flows highlighted the importance of assessing the behaviour of travelling compositional waves before they reach a flow discontinuity, in order to derive and validate analytical models for acoustics generation.

In this work, the propagation of synthetic compositional spots of helium, carbon dioxide and argon injected in a ducted air flow is studied both experimentally and numerically. The Laser Induced Thermal Grating Spectroscopy (LITGS) technique is employed for the first time to time-resolve the density variations induced in the flow by the travelling compositional spots. A 355 nm PIV laser is operated at 500 Hz to generate the thermal grating using biacetyl as an absorber. The LITGS signal frequency encoding the flow properties is acquired with a standard deviation of 2% for the CO₂ and Ar cases, while the helium case highlights the need for a further tuning of the experimental set-up to improve the accuracy.

A CFD procedure is developed in the OpenFOAM framework and employed to simulate the same experimental conditions. Compressible, 3D, unsteady RANS simulations are performed with the solver *reactingFoam* and a modified version of the same, providing an encouraging agreement with LITGS measurements for the CO₂ and Ar cases. On the other hand, the mismatch in the helium case clarifies the need for a more articulate transient boundary condition for the spot injection. The numerical results also show that neither molecular nor turbulent diffusion are playing a relevant role in the investigated compositional waves dispersion, and that the estimated probing volume of LITGS, determined by the employed optical set-up to reduce thermalization effects, is not significantly affecting experimental measurements.

Finally, a theoretical model for the advection of compositional waves is proposed. Assessment against experimental results demonstrates that the dominant contribution to the dispersion of the wave is the differential convection. The formulated theory is also suitable for future inclusion in low-order models of acoustic networks.

Sommario

È stato recentemente dimostrato che disomogeneità composizionali in flussi gassosi accelerati costituiscono una fonte di indirect noise, a sua volta potenziale causa di instabilità termoacustiche in combustori di turbine a gas. Esperimenti condotti presso l'Università di Cambridge su flussi non reagenti in condotti hanno evidenziato l'importanza di valutare le modalità di propagazione delle onde composizionali prima che esse raggiungano una discontinuità di flusso, al fine di derivare e validare modelli analitici per lo studio di fenomeni acustici.

In questo lavoro è presentato lo studio sia sperimentale che numerico della propagazione di disomogeneità composizionali generate iniettando elio, anidride carbonica e argon in un flusso d'aria in un condotto cilindrico. La tecnica Laser Induced Thermal Grating Spectroscopy (LITGS) viene impiegata per la prima volta per misurare variazioni instazionarie di densità del flusso causate dalla convezione dell'onda compositiva. Un laser PIV da 355 nm è impiegato alla frequenza di 500 Hz per generare il grating, mentre il biacetyl è utilizzato come specie assorbente. La frequenza del segnale LITGS che codifica le proprietà del flusso è acquisita con una deviazione standard del 2% nei casi di CO₂ e Ar, mentre l'utilizzo di elio evidenzia la necessità di un'ulteriore messa a punto del set-up sperimentale per migliorare l'accuratezza delle misure.

Una procedura CFD è sviluppata in OpenFOAM ed usata per simulare le stesse condizioni sperimentali. Il solutore *reactingFoam* ed una versione modificata dello stesso sono impiegati per ottenere soluzioni RANS, non stazionarie, 3D e comprimibili. Esse forniscono risultati in buon accordo con le misure LITGS per i casi CO₂ e Ar, mentre la mancata corrispondenza nel caso dell'elio chiarisce la necessità di una condizione al contorno transitoria più articolata per l'iniezione del gas secondario. Le soluzioni numeriche mostrano che né la diffusione molecolare né quella turbolenta giocano un ruolo rilevante nella dispersione delle onde composizionali indagate; inoltre, i risultati suggeriscono che il volume di misura stimato per gli esperimenti LITGS, determinato dal set-up ottico impiegato per ridurre gli effetti di termalizzazione, non influenzi in modo significativo i risultati sperimentali.

Infine, viene proposto un modello analitico per la convezione di onde composizionali. Il confronto con i risultati sperimentali dimostra che il contributo dominante alla diffusione

dell'onda è dato dal meccanismo di shear dispersion. La teoria formulata è inoltre adatta per la futura implementazione in modelli analitici semplificati di sistemi acustici.

Table of contents

List of figures	ix
List of tables	xiii
Frequently used symbols	xiv
1 Introduction	1
1.1 Motivation	1
1.1.1 Aircraft noise	2
1.1.2 Combustion noise	4
1.2 Background	6
1.2.1 Studies on entropy waves	6
1.2.2 Analytical investigations on compositional noise	9
1.2.3 Experiments on compositional noise	10
1.3 Current targets	13
2 Theory	14
2.1 Governing equations	14
2.1.1 Continuity	15
2.1.2 Momentum	15
2.1.3 Energy	16
2.1.4 Species transport	17
2.2 Turbulence modelling	18
2.2.1 Reynolds- and Favre-averaging	18
2.2.2 The closure problem	20
2.2.3 Higher accuracy CFD	25
3 Experimental Investigation with LITGS	26
3.1 Overview of the technique	26

3.2	Experimental set-up	28
3.2.1	Optics	28
3.2.2	Experimental layout	29
3.3	Detection of unsteady compositional spots	30
3.3.1	Procedure	30
3.3.2	Results	32
3.4	Determination of boundary conditions for simulations	34
4	Numerical Simulations	35
4.1	Solvers	35
4.1.1	Steady simulations: <i>rhoSimpleFoam</i>	35
4.1.2	Unsteady simulations: <i>reactingFoam</i> and modified- <i>reactingFoam</i>	36
4.2	Thermophysical properties	37
4.2.1	Transport properties	37
4.2.2	Thermodynamic properties	38
4.2.3	Equation of state	38
4.3	Turbulence model	39
4.4	Methodology	40
4.4.1	Steady state simulation of the entire geometry	40
4.4.2	Domain simplification	44
4.4.3	Injection process	46
4.5	Resulting flow field	48
4.6	Comparison with LITGS	53
4.7	Effects of the sampling method	56
5	Low-order modelling	60
5.1	Formulation	60
5.2	Application to LITGS results	62
5.3	Model sensitivity to the velocity profile	64
6	Conclusions and future work	66
	References	68
	Appendix A Numerical Setup	72
A.1	Mesh convergence study	72
A.2	Numerical schemes	74

List of figures

1.1	ICAO 2014: evolution of cumulative aircraft noise reduction at the source and future goals for commercial aircraft. The symbol size is scaled by the engine bypass ratio. EPNdB: effective perceived noise level in decibels [26].	2
1.2	Breakdown of aircraft noise.	3
1.3	Noise sources for 1960s and 1990s aero-engines [42].	3
1.4	Typical noise sources contribution for a turbojet engine at approach [13]. . .	4
1.5	Pictorial illustration of combustion noise sources in a gas turbine engine: generation of direct and indirect combustion noise [29].	5
1.6	Diagram of the CEG [11] with grid and nozzle thermocouples (T_g and T_n) and pressure measurement p' . P_d^- and P_d^+ are the direct noise pressure waves, P_i^- is the indirect noise pressure wave, σ is the entropy wave . All dimensions in mm, not to scale. Rig diameter 42.6 mm.	7
1.7	Pressure fluctuations downstream of the heating grid for short (left) and long (right) configuration of the CEG. Legend indicates the bulk velocity U in m/s [11].	7
1.8	Sketch of the experimental set-up employed by Rolland <i>et al.</i> [40]. Values of L_c and L are summarized in Table 1.1.	10
1.9	Pressure signals for configuration B obtained by Rolland <i>et al.</i> [40]. Left: experimental acoustic pressure. Center: analytical acoustic pressure. Right: analytical acoustic contributions of direct and indirect noise.	11
1.10	Pressure signals for configuration C obtained by Rolland <i>et al.</i> [40]. Analytical entropic and compositional contributions to indirect noise.	12
2.1	Representation of the Lagrangian (left) and Eulerian (right) approaches for fluid motion study [6].	15

3.1	LITGS technique. Left: schematic view of the interference grating pattern. Right: example of a typical LITGS signal produced by a single pump laser shot [52].	28
3.2	Optical layout [12]. PL: 355 nm pulsed pump laser; CWL: 671 nm continuous solid state laser; PD: photodiode; PMT: photomultiplier; HRM: reflective mirror; BS: beam splitter; BD: beam dumper; CL: crossing lens; CLt: convex lens telescope; DC: delay compensator; S: signal; T: trigger.	29
3.3	Experimental layout: representation of the Entropy Wave Generator with optical access provided by the quartz tube, including the sampled points locations. Dimensions in millimeters, not to scale [12].	29
3.4	Post-processing steps (from left to right: He, CO ₂ , Ar), at the first probed point x_1 . Top: time resolved LITGS traces (peak frequency) for 3 pulses. Bottom: ensemble-averaged (30 pulses) LITGS signals (frequency variation from that of the mean flow).	32
3.5	Detection of compositional spots (from left to right: He, CO ₂ , Ar). Ensemble-averaged secondary gas mass fraction (top) and normalized density variations (bottom), at five axial locations along the quartz tube center line.	33
3.6	LITGS signals acquired in a steady jet of biacetyl-saturated air, CO ₂ , Ar and He. Right: ensemble-averaged signals; inset: zoom on helium signal. Left: corresponding Fourier transform of the signals [12].	33
4.1	Visualization and sketch of the entire computational geometry (axial length scaled by a factor of 0.33 for clarity). Dimensions in mm.	40
4.2	Overview of boundary conditions used performing the steady state simulation of the main air flow in the entire geometry.	42
4.3	Steady state velocity field (top) and close up of the velocity vectors at the expansion region (bottom) for the entire geometry.	43
4.4	Steady state y^+ values on the walls for the entire geometry.	43
4.5	Wall axial velocity profile for a fully developed flow at $Re_D = 5400$: comparison between present OpenFOAM results and data published in [16].	44
4.6	View of the computational grid resulting after the domain reduction. Dimension in mm.	45
4.7	Steady state velocity field for the simplified geometry, using interpolated inlet boundary conditions.	45
4.8	Comparison between the steady state solutions provided by the entire and simplified geometry at the injection location. Right: axial velocity profile. Left: turbulent kinetic energy profile.	46

4.9	Propagation of helium compositional spot: normalized density variations visualized on the symmetry plane at various time steps (time reported in seconds, 0.2 represents the end of the injection).	49
4.10	Propagation of carbon dioxide compositional spot: mass fraction of CO ₂ visualized on the symmetry plane at various time steps (time reported in seconds, 0.2 represents the end of the injection).	50
4.11	Propagation of argon compositional spot: mass fraction of Ar visualized on the symmetry plane at various time steps (time reported in seconds, 0.2 represents the end of the injection).	51
4.12	Visualization of wall vortex generation at different time steps in the argon case: iso- Q surfaces ¹ ($Q = 50000 \text{ 1/s}^2$) coloured by argon mass fraction. Downstream direction from left to right. Time reported in seconds.	52
4.13	Detection of helium compositional spots at five punctual locations downstream. Left: mass fraction of He. Right: normalized density variations. Time traces provided by the standard solver (—), the modified solver (- - -) and ensemble-averaged LITGS traces (dots).	53
4.14	Detection of CO ₂ compositional spots at five punctual locations downstream. Left: mass fraction of CO ₂ . Right: normalized density variations. Time traces provided by the standard solver (—) and the modified solver (- - -); ensemble-averaged LITGS traces (dots).	53
4.15	Detection of argon compositional spots at five punctual locations downstream. Left: mass fraction of Ar. Right: normalized density variations. Time traces provided by the standard solver (—) and the modified solver (- - -); ensemble-averaged LITGS traces (dots).	54
4.16	(a): Schematic top view of the experimental set-up, with estimation of the LITGS grating volume; dimensions not to scale. (b): Computational cross section view showing where the averaging is performed; 100 point sampled on the radius. Dimensions in mm.	56
4.17	Comparison of probing methods, standard <i>reactingFoam</i> . From the top: He, CO ₂ , Ar mass fraction over time at five axial locations downstream of the injection. Left column: punctual probe (—) and average signal on 15 mm along radial direction (- - -). Right column: punctual probe (—), average signal on the entire radius (- - -), area average (- - -) and mass flow average (⋯⋯).	58
5.1	Velocity profile extracted from simulations at the injection axial position.	62

5.2	Compositional wave prediction by the one-dimensional model and comparison with LITGS (dots). Mass flow averaged (solid lines) and area averaged formulation (dashed lines). The first LITGS time trace is smoothed and used as input for the model.	63
5.3	Argon compositional wave predicted by the model in the investigated configuration, for different convective velocity profiles.	65
A.1	Mesh convergence study, helium case, injection period only. (a): Signal of a punctual probe on the center line, 13 cm downstream of the injection. Helium mass fraction (top) and normalized density variation (bottom). (b): Signals averaged over radius at the same axial location.	73
A.2	Numerical schemes used in OpenFOAM for the steady simulations (<i>rhoSimpleFoam</i>).	74
A.3	Numerical schemes used in OpenFOAM for the unsteady simulations (standard and modified <i>reactingFoam</i>).	75

List of tables

1.1	Experimental configurations used by Rolland <i>et al.</i> [40].	11
3.1	Properties of air and biacetyl.	30
3.2	Estimation of the injected mass flow for each gas, used as inlet boundary condition in the simulations.	34
4.1	Relaxation factor used running the steady state simulations with <i>rhoSimpleFoam</i>	36
4.2	Transport properties specified in OpenFOAM solvers.	37
4.3	Laminar and turbulent Schmidt numbers used in the modified- <i>reactingFoam</i> for the three gases.	38
4.4	Thermodynamic properties specified in OpenFOAM for the three gases. . .	38
4.5	Initial and boundary conditions used for the steady state simulation of the main air flow in the entire geometry.	42
4.6	Modifications to boundary conditions done before running the unsteady simulations with <i>reactingFoam</i> , using the steady state solution as initial condition.	47
4.7	Computing time hours required for each case, running on the Darwin Cluster (32 cores).	47
A.1	Mesh convergence study: comparison between the three tested grids.	72

Frequently used symbols

Roman Symbols

f	LITGS signal frequency [Hz]
f_0	LITGS signal frequency of the base flow [Hz]
Re_D	Duct Reynolds number [-]
u	Flow velocity component [m s^{-1}]
W	Molar mass [g mol^{-1}]
X	Molar mass fraction [-]
Y	Mass fraction [-]
y^+	Dimensionless wall distance [-]
\mathcal{R}	Universal gas constant [$\text{J mol}^{-1} \text{K}^{-1}$]

Greek Symbols

$\Delta\rho/\rho_0$	Normalized density variation [-]
ρ_0	Density of the air main flow [kg m^{-3}]

Acronyms / Abbreviations

CFD	Computational Fluid Dynamics
LITGS	Laser Induced Thermal Grating Spectroscopy
RANS	Reynolds Average Navier-Stokes
URANS	Unsteady Reynolds Average Navier-Stokes

Chapter 1

Introduction

1.1 Motivation

The aviation industry is one of the main sectors at the forefront of technology and innovation, playing a relevant impact on the society and providing a vital mean of connection among the world. Over the past fifty years, improvements at the aerospace technology have allowed airlines to increase their management efficiency, thereby enabling to lower they costs; this, in parallel with the liberalization of aviation markets, has been the starting point for a consistent grown in absolute size of the civil airline industry. According to the global air transportation outlook by the International Civil Aviation Organization (ICAO 2013), civil air traffic is projected to grow at an annual rate of 4.6%, resulting in a doubling of air transportation over the next 15 years [25].

This worldwide increase makes it necessary to mitigate its environmental impact in terms of both combustion-sourced pollutant emissions and generation of noise. Nitrogen oxides (NO_x) and carbon oxides (CO_x) have recently become a matter of public concern, since they are strictly linked to health injuries (respiratory inflammation at high level and poisoning) and to global warming and ozone layer depletion phenomena.

Similarly, noise must be reduced. Although individual aircraft have become less noisy over the last thirty years, the massive increase of traffic is causing not only environmental damages, but also health injuries to citizens living near airports: due to its intermittent nature, aircraft noise has both immediate effects (such as annoyance and physiological changes) and longer term effects, e.g. hearing damage, speech and sleep interference [13].

For these reasons, in 2000 a number of aviation industries drew up the Advisory Council for Aeronautics Research and Innovation in Europe (ACARE) [1]; it set common targets aimed to mitigate the environmental impact of the aviation industry by the year 2020. Specifically, the industry sponsored *ACARE 2020* objectives were defined as: an 80% and

50% reduction in nitrous oxides(NO_x) and carbon dioxide (CO_2) emissions respectively, plus a 50% reduction in external noise emissions.

More recently, given the forecast growth in the aviation industry, new goals have been set towards 2050. In the framework of the so called *Flightpath 2050* program, ACARE set new targets for aerospace technologies and procedures (again relative to the capabilities of typical new aircraft in 2000). In particular, objectives can be summarized in a 75% reduction in CO_2 emissions per passenger kilometer, a 90% reduction in NO_x emissions plus a 65% decrease of the perceived noise emission of flying aircraft [2].

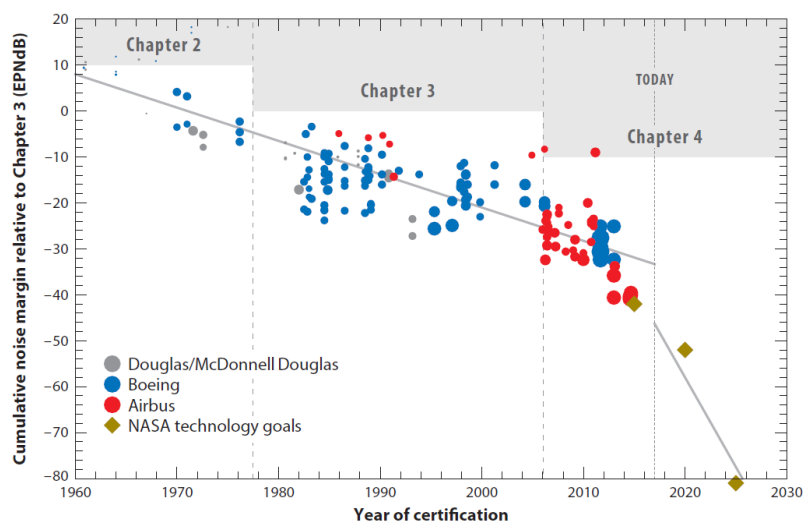


Fig. 1.1 ICAO 2014: evolution of cumulative aircraft noise reduction at the source and future goals for commercial aircraft. The symbol size is scaled by the engine bypass ratio. EPNdB: effective perceived noise level in decibels [26].

1.1.1 Aircraft noise

Aircraft noise is a pollution coming from many components and sources during various phases of a flight, but the main contributors are the engine and the airframe. The former is contributed by the fan, compressor, combustor, turbine and jet exhaust, while the latter is produced by airflow over lifting bodies, control surfaces (flaps and slats), and around the landing gears.

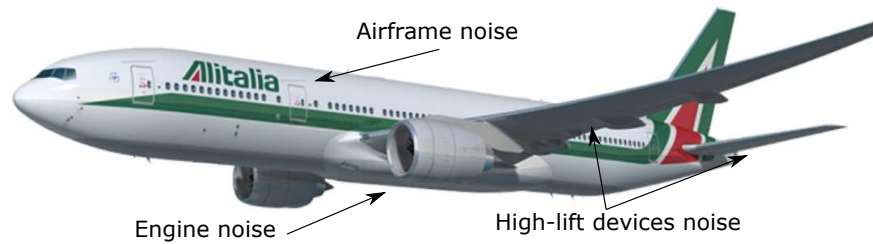


Fig. 1.2 Breakdown of aircraft noise.

The mentioned sources contribute to the overall noise depending on the engine and aircraft design, as well as on the operating condition. Referring to the noise produced in proximity of airports, during take-off the engines operate at full thrust so the jet is the main source; at approach, the most of noise comes from the airframe and specifically from the control surfaces used to produce aerodynamic braking [18].

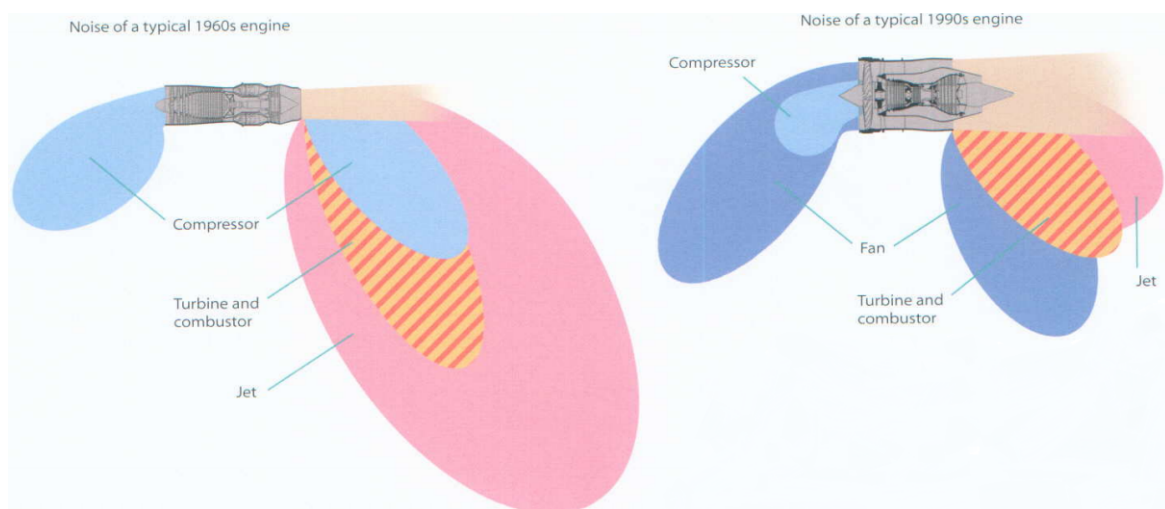


Fig. 1.3 Noise sources for 1960s and 1990s aero-engines [42].

Significant improvements have been carried out during the last decades to reduce the amount of engine noise: the reduction of jet noise has been mainly achieved by employing ultra-high-bypass ratio configurations, while the resulting fan noise has been reduced through effective acoustic liners and complex designs of rotor blades geometries. As a result of these efforts, in modern engines the global noise has been significantly reduced if compared to that produced by those used in the past century (as sketched in Fig. 1.3) but the the combustion noise has become an even more important contributor. Figure 1.4 shows the relative importance of combustion noise for a typical turbojet application [13].

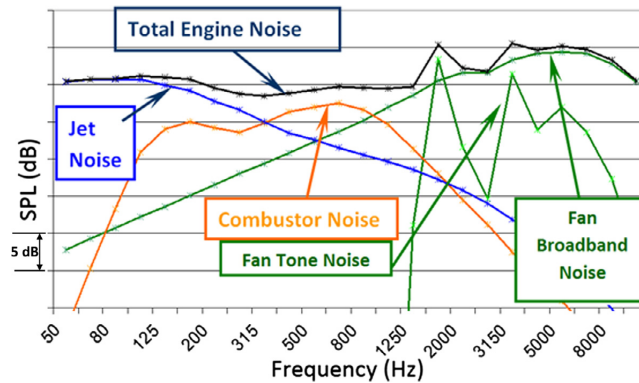


Fig. 1.4 Typical noise sources contribution for a turbojet engine at approach [13].

1.1.2 Combustion noise

Combustion noise (also referred to as *engine-core noise*) appears to be the third dominant source in the whole turbojet engine, after fan and jet. This has been highlighted by the reduction of other noise sources and by the introduction of compact high power density lean premixed prevaporized (LPP) burners, developed and improved to limit NO_x emissions. Those burners operate more unsteadily because of the high sensitivity to disturbances in the turbulent environment of the combustion chamber. Such unsteady fluctuations are the cause of two unwanted phenomena in aero-engines: combustion noise, propagated through the turbine stages and the nozzle, and thermoacoustic instabilities [26]. The latter issue occurs when the heat released by the flame is sufficiently in phase with the acoustic waves, which are reflected at the boundaries and generated at the turbine inlet section. Pressure oscillations reaching a resonant frequency can cause serious structural damage, resulting in a reduction of combustor lifetime by a factor of two or more [13]. The total amount of noise radiated by a gas turbine combustor and the mentioned instability phenomena can be caused by direct and indirect mechanisms.

The direct noise sources are related to the unsteady process of volumetric expansion and contraction in the flame region; this is generated by the fluctuation of heat release rate associated with the chemical reaction, producing pressure perturbations that can be partially transmitted, reflected or dissipated at the combustion chamber boundaries [49].

The indirect combustion noise, firstly identified in the seventies, represents an induced noise-source mechanism that arises from the interaction between non-acoustic perturbation exiting the combustion chamber and downstream engine components. Specifically, when a fluid with a non-uniform temperature, vorticity or chemical composition experiences a velocity gradient (such as when it is convected through the choked nozzle at the combustor outlet) an additional pressure disturbance is generated [13].

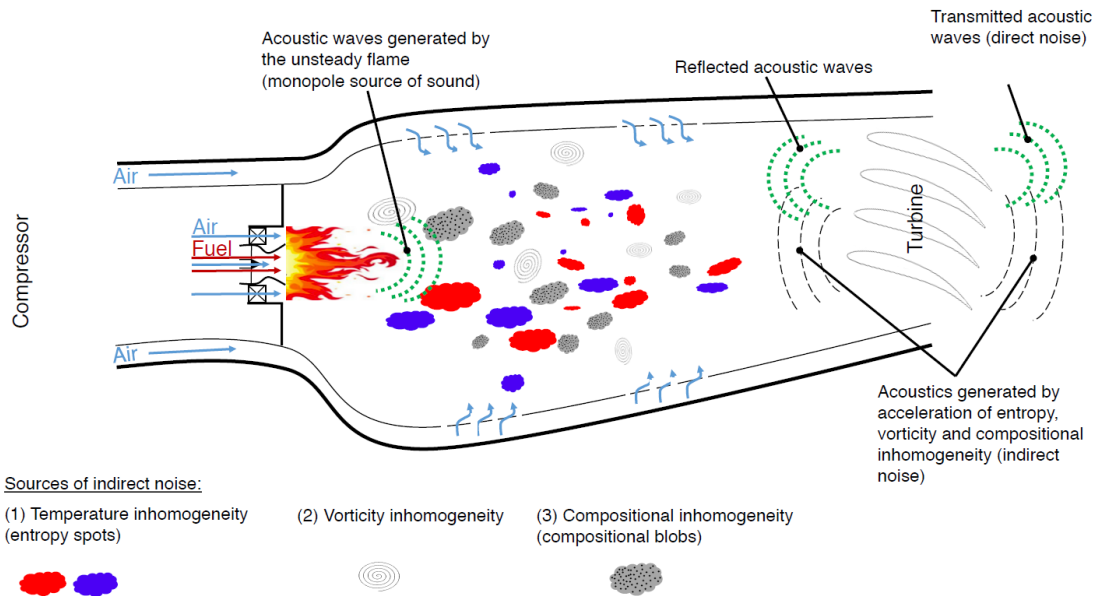


Fig. 1.5 Pictorial illustration of combustion noise sources in a gas turbine engine: generation of direct and indirect combustion noise [29].

Spatial and temporal variations of the combustion rate produce hot and cold spots which are convected with the mean flow; since those spots have a different entropy to that of the surrounding flow, this mechanism is also referred to as *entropy noise*. The combustion process also generates unsteady shear leading to vorticity perturbations, which give rise to pressure disturbances as they are accelerated through the turbine nozzle guide vane. Common to the two previous indirect noise sources there is the fact that they would be present even if convected by a chemical homogeneous flow; this is usually not the case of real engines, since compositional inhomogeneities can arise from incomplete mixing or reactions in the flame region and air dilution of the combustion product after the recirculation zone [26].

Acceleration of the discussed inhomogeneities results in pressure waves that propagate both upstream (from where they can be reflected) and downstream of the first turbine stage, contributing to the overall noise emission. Such waves are considered to be the key feedback mechanism for a very low frequency combustion instability known as 'rumble', which may occur at the start-up of the engine at sub-idle or idle conditions [15].

1.2 Background

1.2.1 Studies on entropy waves

Indirect noise generated by accelerated entropy fluctuations through nozzles was analytically studied by Marble & Candel in the seventies [31]. Starting from the governing equations for a one-dimensional, adiabatic flow with non-uniform entropy and decomposing the flow variables into their mean (in time) and fluctuating components, they defined the first set of transfer functions governing the transmission and reflection of acoustic and entropy waves. Their theory was restricted to low frequency perturbation, e.g. to nozzles that can be considered compact in respect of the perturbations wavelength.

In a real combustion chamber, it is complicated to separate direct and indirect noise; thus, the separation of the two contributions to the overall noise emission has been the focus of theoretical, experimental and numerical studies. One of the main obstacles is the lack of clear data linking entropy and pressure fluctuation caused by real flame dynamics.

At the German Aerospace Centre (DRL), Bake *et al.* [5] overcame this problem developing the first reference case for direct and indirect noise studies: the Entropy Wave Generator (EWG) rig, where entropy waves were produced via pulsating Joule heating of wires. The consequent pressure fluctuations were captured downstream of a nozzle, which could work in choked or unchoked conditions depending on the actual mass flow.

Those experiments led to numerous attempts to build corresponding numerical models. Mühlbauer *et al.* [35] performed compressible URANS simulations, achieving a good agreement with experimental results only after developing a complex reflection coefficient as acoustic boundary condition. Duran *et al.* [14] employed the Euler–Maruyama method, concluding that direct noise was much more significant than indirect noise in subsonic regime. On the contrary, Lourier *et al.* [28], by extending the work by Mühlbauer *et al.*, inferred that the indirect contribution was the main noise source and that the shape of the entropy wave has a strong effect on the resulting indirect noise peak, which resulted lower if generated by a shallower temperature gradient. The mentioned works highlight how those results still remained unclear; this is mainly due to the modelling of the inlet and outlet boundaries, that greatly affect numerical results and requires reflection coefficients to be artificially adjusted to fit experimental results.

To verify the results obtained by the DRL, similar rigs were developed in Oxford [22] and Cambridge. The Cambridge Wave Generator (CEG), described in De Domenico *et al.* [11], allowed to produce synthetic hot spots by pulsating current through a heating device; as sketched in Fig. 1.6, these were convected by a controlled air flow and then accelerated through an orifice plate. The experimental set-up is flexible: the total length of the duct

could be adjusted to modify the acoustic round-trip; specifically, the longest configuration allowed the hot spot produced by a 10 ms heat pulse to reach the acceleration location after the the heating device is turned off. That way, a full separation of direct and indirect noise was achieved, as can be noticed in Fig. 1.7. This specific application allowed to investigate the upstream propagating entropy noise for the first time.

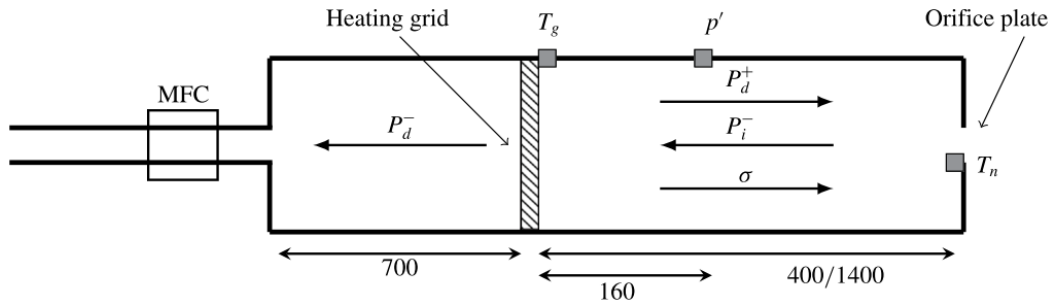


Fig. 1.6 Diagram of the CEG [11] with grid and nozzle thermocouples (T_g and T_n) and pressure measurement p' . P_d^- and P_d^+ are the direct noise pressure waves, P_i^- is the indirect noise pressure wave, σ is the entropy wave. All dimensions in mm, not to scale. Rig diameter 42.6 mm.

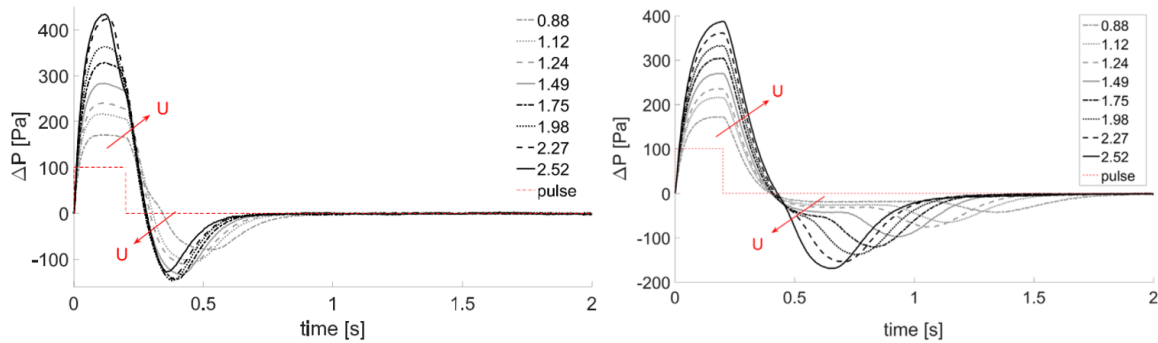


Fig. 1.7 Pressure fluctuations downstream of the heating grid for short (left) and long (right) configuration of the CEG. Legend indicates the bulk velocity U in m/s [11].

Results obtained by the CEG were also compared to URANS compressible simulations carried out by Rodrigues *et al.* ([39],[38]) in the OpenFOAM framework, showing how the separation of the direct and indirect sources could be predicted, but also clarifying the need for more sophisticated acoustic boundary conditions for the computational domain.

Experimental work by De Domenico *et al.* was extended by Rolland *et al.* [41]. They took into account acoustic reflection occurring in the Cambridge EWG experiments, producing and validating a one-dimensional analytical model for direct and indirect noise generation and reverberation in a low frequency framework.

In an attempt to research indirect combustion noise in more realistic environments, Gaetani *et al.* [19] developed a rig using a realistic HP turbine stage at Politecnico di Milano.

Periodic entropy perturbations were generated via a two way rotary valve and an electric heater, alternatively releasing hot and cold air spots. Temperature fluctuations exceeding 10 K at a frequency of 100 Hz were successfully achieved.

Common to the presented references there was a main focus on the generated indirect noise and to its acoustic analysis, whereas not much attention has been devoted to the characterization of the attenuation of entropy waves. Sattelmayer [44] first developed an analytical model for entropy wave dispersion caused by combustor aerodynamics. He concluded that, if dispersion is taken into account, the entropy waves effect can be neglected in stability analysis; this is due to the strong mixing and turbulence intensity inside a real chamber. The work by Morgans *et al.* [34] can be considered one of the first attempt to study entropy waves dispersion using CFD, and specifically direct numerical simulations (DNS). Morgans *et al.* studied the advection of a Gaussian temperature perturbation in a turbulent, incompressible, fully developed channel flow between two parallel plates. This way, the importance of the effect of a mean velocity profile that varies across the section (causing different residence times of disturbances in different regions) was highlighted, and a one-dimensional transfer function of entropy waves magnitude was suggested. In contrast with Sattelmayer, they also concluded that entropy wave dissipation is negligible in for representative gas turbines flows, such that significant entropy wave strength could remain at the combustor exit (specifically at low frequencies, that are relevant to combustion stability). Within the same research group, Xia *et al.* [55] studied the advection of entropy waves by LES simulation of an adapted Siemens GT combustor; they highlighted how the effect of more complex swirl-stabilized configurations still needs to be investigated through both numerical and experimental investigation.

More recently, Giusti *et al.* [20] investigated the entropy wave propagation and dispersion in a small scaled cylindrical rig, using both experiments and LES simulations. Results demonstrated that the amplitude of entropic fluctuations decays as function of wave parameters described by a local Helmholtz number, based on the entropy wavelength and the rig radius. Furthermore, assessment between experimental and numerical results showed agreement between decay rates in terms of both magnitude and phase of the entropy wave, and that the contribution of differential convection is dominant in the diffusion process when low frequency waves are considered. Giusti *et al.* also pointed out that the geometry and velocities investigated are far from those in a real engine application; thus further work is advised in order to fully understand every aspect of engine core noise mechanisms.

1.2.2 Analytical investigations on compositional noise

In the afore-mentioned studies regarding entropy waves, the perturbations advected with the mean flow were modelled with the restriction to a single-component gas, without considering the effects of inhomogeneities in mixture composition on the indirect noise generation. In particular, compositional inhomogeneities could arise in a real engine configuration because of incomplete mixing during the combustion process (stratification), products dilution or, in general, variations in combustor exhaust gas composition; mentioned inhomogeneities can become increasingly important in modern compact low emission burners, that aim to provide high-power-density cores.

The existence of indirect noise generated by accelerated mixture inhomogeneities was first identified analytically by Ihme [26]. Starting from the one-dimensional compact nozzle theory proposed by Marble & Candel [31], Ihme extended it to examine the effects of mixture fluctuations on the acoustic response of subcritical isentropic nozzles. Casting the linearised Euler equation for perturbations of the mass flow rate, total sensible enthalpy and mixture fraction (neglecting vortical disturbances), the jump conditions across the nozzle are obtained; those equations are then related to the flow primitive state variables through the total enthalpy definition, equation of state and Gibbs' equation for a multicomponent gas. This way, the upstream and downstream propagating acoustic, entropy and compositional waves expressions are recovered, as also the corresponding linear set of transfer functions for a subsonic compact nozzle.

Magri *et al.* [30] extended the analytical work by Ihme to one-dimensional, non-compact, isentropic, supersonic and subsonic nozzles for a calorically perfect gas mixture. They introduced the chemical potential function, Ψ , defined as:

$$\Psi = \frac{1}{T c_p} \sum_{i=1}^{N_s} g_i(T, p) \frac{\partial Y_i}{\partial Z} \quad (1.1)$$

where g_i and Y_i are the specific Gibbs free energy and mass fraction of one of N_s species, and Z is the mixture fraction. Ψ depends on pressure and temperature, so it changes across a nozzle. This way, a new term was identified in the governing equations proposed by Marble & Candel acting as a new source of noise in presence of mean flow gradients, denominated "compositional noise". Magri *et al.* applied this theory to the limit case of a compact nozzle for a *n*-dodecane mixture, finding that compositional noise can also exceed the entropy noise for supercritical nozzle at lean mixtures (which corresponds to real engines operative conditions). They also performed an analysis to identify the individual species that contribute most strongly to the indirect signal; since it is differences the chemical potential across the nozzle that generate pressure disturbances, it was found that the most acoustically efficient

species are those having both high mass fraction values, high mass fraction gradients and molecular weights strongly differing from that of the surrounding mixture.

By extending the mentioned theory, Magri [29] later proposed an acoustic model for unsteady, non-compact, subsonic and supersonic nozzle flows for multicomponent gases with variable composition and specific heat capacity, managing to separate the entropic and compositional sources of indirect noise. Specifically, Magri found out that compositional inhomogeneities cause indirect noise not only through the chemical potential function, but also introducing specific heat capacity variations that modify the entropy perturbation. Physically, this can be interpreted as follows: not only density variations produce indirect noise through entropy mechanism or the previously defined chemical potential, but also through heat-capacity variations: such a source is caused by the tendency of the accelerated compositional spot to contract/expand with a different rate than the surrounding fluid.

1.2.3 Experiments on compositional noise

Low frequency compositional noise has been firstly investigated experimentally by Rolland *et al.* [40], employing the set-up represented in Fig. 1.8 (which is derived from the Cambridge Wave Generator described in [11] and reported in Fig. 1.6). The experiment consisted of detecting direct and indirect noise generated by the injection of a fluctuating mass flow of helium into a main flow of air. The acceleration of the flow was achieved by an acoustically compact choked nozzle at the downstream end of the rig and pressure signals were acquired upstream of the flow discontinuity. Experiments were run with a number of different mass flows of air and helium, adopting a variable distance between the injection location and the nozzle itself (L_c in Fig. 1.8); values used are summarized in Table 1.1 together with the resulting total duct length, L .

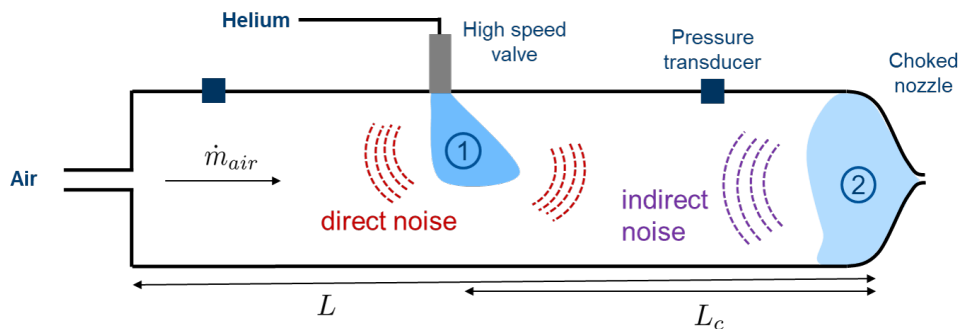


Fig. 1.8 Sketch of the experimental set-up employed by Rolland *et al.* [40]. Values of L_c and L are summarized in Table 1.1.

Table 1.1 Experimental configurations used by Rolland *et al.* [40].

Configuration	Convective length, L_c [m]	Total duct length, L [m]
A	61.65	62.6
B	0.65	1.6
C	0.05	1.6

Results were used to validate an analytical one-dimensional model devoted to predict the pressure signal resulting from the overlapping of direct, entropic and compositional noise sources. Specifically, starting from the assumption of one-dimensional linear perturbations induced by the injection (assumed to be a square pulse), the model made use of the transfer function introduced by Marble & Candle [31] for entropy noise and the transfer function for compositional noise identified by Magri [30], adding a model developed *ad hoc* for the employed experimental configuration to take into account acoustic reverberation and characteristic lengths and time constants of the rig. The three configurations were specifically designed in order to assess the validity of the direct noise predictions (A), to validate the reverberation model and decay prediction (B) and to verify the applicability of the indirect noise model in almost complete absence of dispersion of the compositional wave (C).

Figure 1.9 reports the results obtained for the configuration B: the experimental acoustic pressure is reported on the left hand side, the analytically predicted total noise is reported at the center, and the analytical direct and indirect contributions extracted from the model are reported on the right hand side. The analytical indirect pressure signal can also be decomposed to visualize the individual contribution of entropy and compositional noise; this step is reported in Fig. 1.10, which refers to configuration C (minimized wave dispersion).

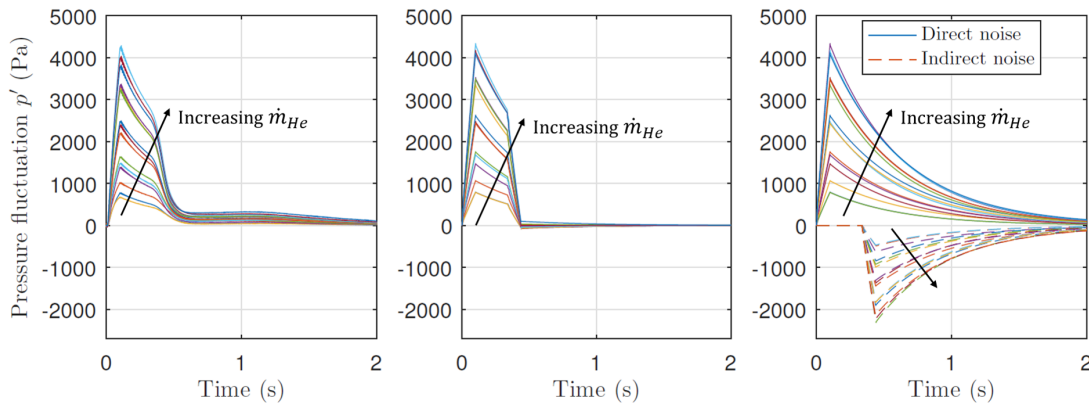


Fig. 1.9 Pressure signals for configuration B obtained by Rolland *et al.* [40]. Left: experimental acoustic pressure. Center: analytical acoustic pressure. Right: analytical acoustic contributions of direct and indirect noise.

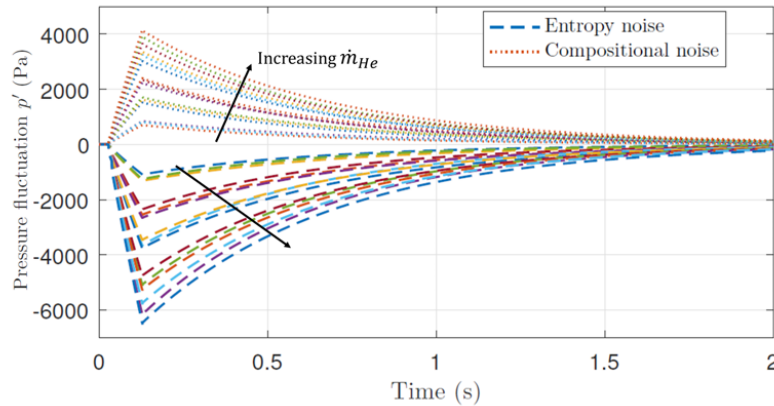


Fig. 1.10 Pressure signals for configuration C obtained by Rolland *et al.* [40]. Analytical entropic and compositional contributions to indirect noise.

Comparing the analytical and the experimental results, Rolland *et al.* highlighted what follows:

- for the employed configuration, compositional acoustic pressure has the same order of magnitude of the entropic source but, since helium was used, they have opposite sign;
- the model under-estimated the direct noise produced by helium injection. This required an empirical correction of the model based on the experimental values. The discrepancy was attributed to noise sources not taken into account in the 1D theory: in fact, the injection is expected to produce more complicated fluid-dynamic phenomena (such as formation of a jet and vorticity generation) that were not considered;
- the indirect noise can generally be well predicted using the transfer function defined by Magri *et al.* [30]. However, indirect noise peak is under-estimated in configuration B (where the convective length for the compositional wave is 0.65 m), and the predictions showed a more sharp increase if compared to the experiments, that exhibited a smoother signal. This is expected, since the diffusion and dispersion of the advected compositional wave were not taken into account: those cause the real impinging wave profile to be more similar to a Gaussian rather than a square pulse.

1.3 Current targets

Experimental and theoretical work by Rolland *et al.* on the Cambridge Entropy Generator managed to prove the existence and separate the contributions of direct and indirect compositional noise in a system with well controlled boundary and operating conditions. They also highlighted the importance of estimating the real behaviour of the compositional waves before they reach the flow discontinuity, since this proved to influence the resulting acoustic pressure signal even in the adopted simplified set-up. Such a step is fundamental to improve the accuracy of analytical models and provide a better understanding about the physics of the convection and mixing process, followed by acoustics generation.

Professor Hochgreb's group is currently working on the development, comparison and validation of experimental techniques and numerical tools to investigate the advection and dispersion process of synthetic compositional waves generated in small scaled rigs, for future derivation and validation of analytical models for low-order acoustic networks.

The present report (i) assesses the feasibility of employing the LITGS technique to time-resolve the advection of unsteady compositional spots generated in a set-up derived by the Entropy Wave Generator and (ii) investigates if the open-source CFD software OpenFOAM is capable of producing comparable results. A preliminary analytical model is also formulated, with the aim of providing theoretical evidence. The modelling activity, which has been the main focus of the author's work, helped to provide a better understanding of the fluid-dynamics phenomena governing the problem and highlighted the needs for future improvements in both the numerical and experimental set-up.

The long term objectives are to develop a direct and indirect noise numerical predictive tool for generation due to synthetic, compositional and flame sources.

Chapter 2

Theory

2.1 Governing equations

The governing equations for fluid flows represent mathematical statements of the basic conservation laws of physics [50]:

- the mass of a fluid is conserved;
- the rate of change in momentum equals the sum of the forces on a fluid particle (Newton's second law);
- the rate of change of energy is equal to the sum of the rate of heat addition to and the rate of work done on a fluid particle (first law of thermodynamics).

As long as the analysis of fluid flows is led at macroscopic length scales ($\sim 1 \mu m$ or larger), the molecular structure of the matter and molecular motions may be ignored. This is known as the *continuum theory*, and allows to describe the behaviour of the fluid in terms of macroscopic properties such as pressure, velocity, density and temperature and their time and space derivatives [6].

It is possible to consider fluid flows comprised of a large number of finite sized fluid particles having their own properties (such as mass, momentum and energy); this is known as the Lagrangian description of fluid motion, and allows to write mathematical laws for each fluid particle. On the other hand, the flow properties can be considered to change at infinitesimal fluid elements that are fixed in time and space; those elements represent fixed control volumes where the governing equation can be obtained simply by writing differential balances of each relevant quantity. This is known as the Eulerian approach: it fits perfectly with the the standard CFD methodology, since the infinitesimal control volumes correspond to the elements of the mesh.

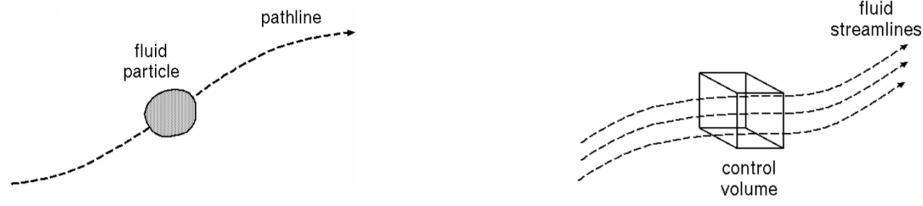


Fig. 2.1 Representation of the Lagrangian (left) and Eulerian (right) approaches for fluid motion study [6].

The general conservation equation for a quantity ϕ can be written in differential form and vector notation as:

$$\underbrace{\frac{\partial}{\partial t}(\rho\phi)}_{\text{time accumulation}} + \underbrace{\nabla \cdot (\rho\mathbf{u}\phi)}_{\text{convective term}} = \underbrace{\nabla \cdot (C_d\nabla\phi)}_{\text{diffusive term}} + \underbrace{S_\phi}_{\text{source term}} \quad (2.1)$$

where C_d is the diffusion coefficient. This equation represents the balance per unit of mass of surface fluxes, rate of change, sources and sinks of the quantity ϕ into the elementary fluid control volume.

2.1.1 Continuity

The continuity equation for compressible flows can be obtained from Equation 2.1 by setting $\phi = 1$. Assuming no source terms and that mass is not diffused, but only convected and accumulated, we obtain:

$$\frac{\partial}{\partial t}\rho + \nabla \cdot (\rho\mathbf{u}) = 0 \quad (2.2)$$

2.1.2 Momentum

The vectorial form of the momentum conservation equation represents the balance between the accumulated, convected and diffused momentum and the sum of the external forces acting on the control volume. Setting $\phi = \mathbf{u}$ in Equation 2.1 we obtain [24]:

$$\frac{\partial}{\partial t}(\rho\mathbf{u}) + \nabla \cdot (\rho\mathbf{u} \otimes \mathbf{u}) = \nabla \cdot \boldsymbol{\tau} - \nabla p + \rho\mathbf{g} \quad (2.3)$$

The balance includes the effect of pressure forces, as well as gravitational effects resulting from \mathbf{g} . Additionally, momentum is also transported due to molecular phenomena based on velocity gradients: the term $(\nabla \cdot \boldsymbol{\tau})$ represents the additional flux of momentum through the control surface caused by the shear-rate tensor, and it is known as *shear stress*.

In the present formulation, the nine components τ_{ij} of the shear-rate tensor $\boldsymbol{\tau}$ are not known; they need to be expressed by auxiliary equations, which depend on the behaviour of the fluid. Only six components are independent if the fluid is assumed isotropic. In a Newtonian compressible fluid, the viscous stresses are proportional to the rates of deformation through two constants of proportionality: the (first) dynamic viscosity, μ , relates stresses to linear deformation, and the second viscosity, λ , relates stresses to volumetric deformation. The nine components of $\boldsymbol{\tau}$, of which six are independent, are given by:

$$\tau_{ij} = \mu \left(\frac{\partial u_i}{\partial x_j} - \frac{\partial u_j}{\partial x_i} \right) - \delta_{ij} \lambda \frac{\partial u_i}{\partial x_i} \quad (2.4)$$

When working with gases, the second viscosity can be assumed to be $\lambda = -\frac{2}{3}\mu$ [45]. Liquids are incompressible, so the continuity equation is $\nabla \mathbf{u} = 0$ and the second term in the definition of $\boldsymbol{\tau}$ components is zero. This way, the unknown in the presented momentum equation (2.3) have been expressed as functions of \mathbf{u} and its space derivatives.

2.1.3 Energy

It is possible to write the energy balance of the control volume in terms of total energy, mechanical energy, internal energy, temperature or sensible enthalpy [24]. In any case, the change of energy in the elementary control volume must take into account the rate of accumulation, the fluxes entering and leaving the volume, net addition by conduction, the work done by the system on surroundings and possible extra heat sources. The conservation equation for total energy per unit of mass (including the thermal, e , and kinetic contributors) is here presented:

$$\frac{\partial}{\partial t} (\rho e + \frac{1}{2} \rho |\mathbf{u}|^2) = \underbrace{-\nabla \cdot (\rho \mathbf{u} (e + \frac{1}{2} |\mathbf{u}|^2))}_{\text{convection}} \underbrace{-\nabla \cdot \mathbf{q}}_{\text{diffusion}} \underbrace{+\rho (\mathbf{u} \cdot \mathbf{g})}_{\text{gravity}} \underbrace{-\nabla \cdot (p \mathbf{u})}_{\text{pressure}} \underbrace{-\nabla \cdot [\boldsymbol{\tau} \cdot \mathbf{u}]}_{\text{viscous forces}} \underbrace{+\rho S}_{\text{heat sources}} \quad (2.5)$$

where the diffusion term is derived using the Fourier law: $-\nabla \cdot \mathbf{q}$, being $\mathbf{q} = -k \nabla T$ (k is the thermal conductivity).

2.1.4 Species transport

When the problem deals with multi-species flows, additional physics need to be modelled. Specifically, the material transport can be studied casting N_s auxiliary equations in the conservative form, where N_s is the number of chemical species involved in the problem; each equation is obtained by setting $\phi = Y_i$ in Equation 2.1, where Y_i is the mass fraction the i -th species:

$$\frac{\partial}{\partial t}(\rho Y_i) + \nabla \cdot (\rho \mathbf{u} Y_i) = -\nabla \cdot \mathbf{J}_i + S_i \quad (2.6)$$

In the presented equation S_i is the source term for the species i , derived by chemical reactions or any user-defined sources. \mathbf{J}_i is the diffusion flux of the species i arising from gradients of concentration and temperature. The molecular transport processes that can cause diffusive fluxes are quite complicated, and a full description was proposed by Williams *et al.* [53]. A common simplification of the diffusive term is the Fick's law [17] (also called "dilute approximation"), leading to:

$$\mathbf{J}_i = -\rho D_{m,i} \nabla Y_i - D_{T,i} \frac{\nabla T}{T} \quad (2.7)$$

To avoid complications in the development of the presented theory, thermal (Soret) diffusion is neglected, thus:

$$\mathbf{J}_i = -\rho D_i \nabla Y_i \quad (2.8)$$

This expression of \mathbf{J}_i is known as the binary diffusion approximation [37], where the mass diffusion coefficient $D_{m,i}$ (now denoted simply as D_i) is computed for every species i with respect to an abundant species, for instance N_2 when dealing with lean combustion processes or pollutant emissions dispersion in air.

Equation 2.6 is usually solved for $(N_s - 1)$ species, while the N_{th} mass fraction is determined as one minus the sum of the $(N_s - 1)$ solved mass fractions; this ensures that the mass fractions sum to one, and by selecting N_{th} as the species with the overall largest mass fraction, the numerical error is minimized [4].

The governing theory can be further simplified by assuming a single diffusion coefficient for every species, leading to: $\mathbf{J}_i = -\rho D \nabla Y_i$. The product ρD , like the dynamic viscosity, is usually taken as a function of temperature, pressure and/or composition.

2.2 Turbulence modelling

The present work deals with numerical simulations of duct flows having local Reynolds numbers ranging from about 2570 to 14000. This range covers transitional and turbulent profiles, thus an overview of turbulence modelling is presented here.

2.2.1 Reynolds- and Favre-averaging

The Navier-Stokes equations allow to resolve every characteristic of a fluid flow (such as vortexes) as long as both spatial and time discretization are fine enough. Since it is really challenging to resolve the flow with all details and physics, the Reynolds averaging approach can be used to simplify the governing equations: this allows to avoid resolving the turbulence scales, simply modelling their effect on the mean flow variables.

Reynolds-averaging is thus based on the separation of mean flow quantities from their fluctuations due to turbulent effects; this means that if a flow has a deterministic character, every flow variable of interest, ϕ , can be expressed as:

$$\phi(t, x) = \bar{\phi}(x) + \phi'(t, x) \quad (2.9)$$

where $\bar{\phi}$ is the mean value and ϕ' is the fluctuating value. Three different averaging concepts were introduced by Reynolds [24]:

- time averaging, that can be used for stationary turbulent flows:

$$\bar{\phi}(x)_T = \lim_{T \rightarrow \infty} \frac{1}{T} \int_t^{t+T} \phi(t, x) dt \quad (2.10)$$

- spacial averaging, appropriate for homogeneous turbulent flows:

$$\bar{\phi}(x)_V = \lim_{V \rightarrow \infty} \frac{1}{V} \iiint_V \phi(t, x) dV \quad (2.11)$$

- ensemble averaging, generally applicable to properties sampled in N identical series, where $\phi_n(t, x) = \phi(t, x)$ at the n -th series:

$$\bar{\phi}(t, x)_E = \lim_{N \rightarrow \infty} \frac{1}{N} \sum_{n=1}^N \phi_n(t, x) \quad (2.12)$$

Applying time averaging to non-stationary flows (where also mean properties changes with time) one gets:

$$\phi(t, x) = \bar{\phi}(x, t) + \phi'(t, x) \quad (2.13)$$

$$\bar{\phi}(t, x)_T = \lim_{T \rightarrow \infty} \frac{1}{T} \int_t^{t+T} \phi(t, x) dt \quad (2.14)$$

$$\lim_{T \rightarrow \infty} \frac{1}{T} \int_t^{t+T} \phi'(t, x) dt = 0 \quad (2.15)$$

Applying the same decomposing and average procedure to the compressible continuity equation (2.2), we have:

$$\frac{\partial}{\partial t} \bar{\rho} + \nabla \cdot (\bar{\rho} \bar{\mathbf{u}} + \overline{\rho' \mathbf{u}'}) = 0 \quad (2.16)$$

where the extra term $\overline{\rho' \mathbf{u}'}$ is not equal to zero since variations of velocity and density are not correlated in a compressible flow. This brings about the problem of approximating the correlation between ρ' and u'_i , and this would be even more complex for non-linear terms arising in the momentum equation.

For this reason, it is useful to employ a non-physical, yet effective mathematical procedure, called *Favre-averaging*. It decomposes flow variables into a mean component weighted on density, $\tilde{\phi}$, plus a fluctuating component, ϕ'' , such that $\phi = \tilde{\phi} + \phi''$. Specifically:

$$\tilde{\phi}(t, x) = \frac{\overline{\rho \phi}}{\bar{\rho}} = \frac{1}{\bar{\rho}} \lim_{T \rightarrow \infty} \frac{1}{T} \int_{\tau}^{\tau+T} \rho(\tau, x) \phi(\tau, x) d\tau \quad (2.17)$$

By applying this definition to the non-linear term in the Reynolds-averaged continuity equation (2.16) it can be shown that:

$$\bar{\rho} \tilde{u}_i = \overline{\rho u_i} = \bar{\rho} \tilde{u}_i + \overline{\rho' u'_i} \quad (2.18)$$

Following this procedure, a modified set of governing equations is defined [50]:

Continuity

$$\frac{\partial}{\partial t} \bar{\rho} + \frac{\partial}{\partial x_i} (\bar{\rho} \tilde{u}_i) = 0 \quad (2.19)$$

Here it can be noticed how the dependent variable is the momentum per unit volume, instead of the velocity. This is sensible from a physical perspective.

Momentum

$$\frac{\partial}{\partial t} (\bar{\rho} \tilde{u}_i) + \frac{\partial}{\partial x_j} (\bar{\rho} \tilde{u}_i \tilde{u}_j + \bar{p} \delta_{ij}) = \frac{\partial}{\partial x_j} (\bar{\tau}_{ij} - \overline{\rho u'_i u'_j}) \quad (2.20)$$

where the term $\overline{\rho u_i'' u_j''}$ is the Favre-averaged Reynolds stress tensor.

Energy

$$\begin{aligned} \frac{\partial}{\partial t} \left[\bar{\rho} \left(\tilde{e} + \frac{1}{2} \tilde{u}_i \tilde{u}_i \right) + \frac{1}{2} \overline{\rho u_i'' u_i''} \right] + \frac{\partial}{\partial x_j} \left[\bar{\rho} \tilde{u}_j \left(\tilde{e} + \frac{1}{2} \tilde{u}_i \tilde{u}_i \right) + \frac{\tilde{u}_j}{2} \overline{\rho u_i'' u_i''} \right] = \\ \frac{\partial}{\partial x_j} \left[\tilde{u}_i \left(\tau_{ij} - \overline{\rho u_i'' u_j''} \right) - \bar{q}_j \right] \\ + \frac{\partial}{\partial x_j} \left[\underbrace{-\overline{\rho u_j'' e''}}_{\text{Turbulent transport of heat}} \underbrace{-\frac{1}{2} \overline{\rho u_j'' u_i'' u_i''}}_{\text{Turbulent transport of kinetic energy}} + \underbrace{\overline{\rho u_i'' \tau_{ij}}}_{\text{Molecular diffusion of turbulent energy}} \right] \end{aligned} \quad (2.21)$$

When dealing with compressible RANS simulations in OpenFOAM, variables will be, by default, assumed to be Favre-averaged.

2.2.2 The closure problem

As a result of either Reynolds- or Favre-averaging procedures, new terms in the governing equations appear. Referring to the Reynolds-averaging procedure for incompressible fluids, the extra terms $\overline{\rho u_i' u_j'}$ would need to be computed in the momentum equation: this is known as the *Reynolds stress tensor*, as it is also visible in the Favre-averaged momentum equation previously reported. Further, extra terms appear also in the energy and species equations, accounting for turbulence transport and diffusion effects.

As a result, the governing theory is now represented by a system with more unknowns than equations, leading to what is called the “closure problem”. Methods used to relate these unknown quantities to known variables are defined as turbulence models, and a brief overview of them is here presented.

2.2.2.1 Reynolds stress models (RSM - ARSM)

This is the most complete classical model to close the RANS governing equations: it introduces a differential equation in the conservative form (2.1) for each Reynolds stress tensor’s component. Such a model offers good accuracy, managing to solve every component of the turbulent transport without being computationally expensive as *Large Eddy Simulations* or *Direct Numerical Simulations*, but usually requires a fine calibration of employed coefficients; this is necessary mainly to have reliable prediction of how the Reynolds stress affects the mean flow variables in terms of turbulent diffusion [9].

A simplified version of the classic model consists in the implementation of auxiliary algebraic equations instead of partial differential equations: this method is known as *Algebraic Reynolds stress model*, and allows a significant computational cost reduction if compared to standard RSM. On the other hand, ARSM gives up accuracy and presents the same calibration requirements.

2.2.2.2 Eddy-Viscosity models: Boussinesq hypothesis

Eddy-Viscosity models for Reynolds- or Favre-averaged turbulent problems rely on the isotropic turbulence hypothesis combined with the *Boussinesq hypothesis*: the latter consists of modelling the Reynolds stress tensor in the same way as the laminar shear rate tensor is defined, thus assuming the turbulent transport of flow properties simply related to mean flow spatial gradients. Referring to the incompressible Reynolds-averaged procedure, the describing equations are usually formulated as:

$$\overline{\rho u'_i u'_j} = -\mu_T \left[\frac{\partial \bar{u}_i}{\partial x_j} + \frac{\partial \bar{u}_j}{\partial x_i} \right] + \frac{2}{3} \delta_{ij} \mu_T \frac{\partial \bar{u}_j}{\partial x_j} \quad (2.22a)$$

$$\overline{u'_i \phi'} = -D_T \frac{\partial \bar{\phi}}{\partial x_i} \quad (2.22b)$$

where D_T is the turbulent diffusivity of the scalar ϕ and μ_T is the turbulent dynamic viscosity, also known as *eddy viscosity*. The closure problem is now reduced to the modelling of the turbulent diffusivity and viscosity: this may be done in a variety of method, casting a different number of conservation differential equations:

- Zero-equation, or algebraic, models rely on the *Prandtl mixing length hypothesis*. This is a turbulent length scale which needs to be modelled to represent the equivalent length of momentum transfer of a fluid particle to those neighbouring. Estimations of mixing length, l_m , can be found in literature (e.g. the Baldwin-Lomax formulation [7]); the eddy viscosity is then computed as.

$$\mu_T = \rho l_m |\nabla \times \mathbf{u}| \quad (2.23)$$

This kind of model is computationally cheap, but works fine only in convection-dominated problems in simply geometries and in absence of strong flow gradients. Further it cannot account for history effects of turbulence, since it is based on local calculations.

- One-equation models (such as the Spalart-Allmaras) add one extra differential equation in conservative form for a turbulence characteristic quantity, usually the turbulent

kinetic energy, k . Once solved, the eddy viscosity is modelled as:

$$\mu_T = \rho l_m \sqrt{k} \quad (2.24)$$

as it can be seen, one-equation models still rely on the mixing length hypothesis, so the transport of turbulent lengths is not considered. However, solving a conservation equation for a turbulence variable allows to keep trace of history effects, thus ensuring a satisfying accuracy in solving free-stream flows.

- Two-equations models include two extra transport equations to represent turbulent properties of the flow. A deeper overview of these models is presented in the next section.

2.2.2.3 Overview of two-equations models

Models like the $k - \varepsilon$ and $k - \omega$ have become a standard in industry, since they can be applied successfully to a variety of fluid-dynamics problems. As previously discussed, the underlying assumption of this model is that turbulence is isotropic.

$k - \varepsilon$ model

This is one of the most commonly used models. The standard formulation proposed by Launder and Spalding [27] closes the RANS governing equations solving two extra PDEs, one for the turbulent kinetic energy, k , and one for the turbulent dissipation rate, ε :

$$\frac{\partial \rho k}{\partial t} + \nabla \cdot (\rho k \mathbf{u}) = \nabla \cdot \left(\frac{\mu_T}{\sigma_k} \nabla k \right) + 2\mu_T \bar{S}_{ij} \cdot \bar{S}_{ij} - \rho \varepsilon \quad (2.25a)$$

$$\frac{\partial \rho \varepsilon}{\partial t} + \nabla \cdot (\rho \varepsilon \mathbf{u}) = \nabla \cdot \left(\frac{\mu_T}{\sigma_\varepsilon} \nabla \varepsilon \right) + 2C_{1\varepsilon} \frac{\varepsilon}{k} \mu_T \bar{S}_{ij} \cdot \bar{S}_{ij} - C_{2\varepsilon} \rho \frac{\varepsilon^2}{k} \quad (2.25b)$$

where $\bar{S}_{i,j} = \partial \bar{u}_i / \partial x_j + \partial \bar{u}_j / \partial x_i$ is the strain rate tensor, and the five adjustable constants have the following standard values: $\sigma_k = 1.00$, $\sigma_\varepsilon = 1.30$, $C_{1\varepsilon} = 1.44$, $C_{2\varepsilon} = 1.92$.

These two equations are solved along with the other RANS equations, and values of k and ε are used to calculate the eddy viscosity and turbulent diffusivity as:

$$\mu_T = \rho C_\mu \frac{k^2}{\varepsilon} \quad (2.26a)$$

$$D_T = \frac{\mu_T}{\rho S c_{turb}} \quad (2.26b)$$

where the constant C_μ is widely assumed to be 0.09 and Sc_{turb} is the turbulent Schmidt number.

A well known limitation of the standard formulation is the inability to integrate the model equations right through to the wall [50]. For this reason, the non dimensional wall distance¹, y^+ of the first grid cell center must be higher than 30, in order to fall within the log-law of the wall. This leads to the need of formulating appropriate wall boundary condition values for the turbulence properties: these are known as “wall functions”, and allow to model the viscous sub-layer effects without resolving it.

$$k = \frac{u_\tau^2}{\sqrt{C_\mu}}; \quad \varepsilon = \frac{u_\tau^3}{0.41y} \quad (2.27)$$

When low Reynolds flows are studied it is complicated to create satisfactory computational grids ensuring $y^+ > 30$, so the boundary conditions above cannot be used and modification to the $k - \varepsilon$ model are required: those were reviewed by Patel *et al.* [36], and are known as “damping functions”. Wall damping needs to be applied to ensure that viscous (laminar) stresses take over from the turbulent Reynolds stresses in the viscous sub-layer adjacent to solid walls, resulting in a correct prediction of velocity gradients in normal direction. The complete formulation of the modified model is not presented here, but it can be found in [50]. Advantages and disadvantages of this model are well portrayed in the mentioned references too.

$k - \omega$ model

Introduced by Wilcox [51], it is an alternative to the $k - \varepsilon$ model presented before. The RANS equations are closed by two PDEs similar to 2.25, but the specific dissipation (or dissipation frequency), ω is used instead of the absolute dissipation, ε . This model is known to perform better in bounded flows, while being very sensitive to free stream turbulent conditions used as inlet conditions [9]. The standard formulation presents the same limit of the $k - \varepsilon$ in terms of y^+ requirements if no damping functions are implemented to correctly account for the viscous sub-layer properties.

¹The non-dimensionalized wall coordinates are defined as:

$$y^+ = y \sqrt{\frac{\tau_{wall}}{\rho_{wall}}} \frac{1}{v_{wall}}; \quad u^+ = u/u_\tau = u / \sqrt{\frac{\tau_{wall}}{\rho_{wall}}}$$

$k - \omega$ SST model

The SST two equation turbulence model was introduced in 1993 by Menter [32], and it has become very popular for a variety of applications in industry. This model allows to switch between a $k - \omega$ and a $k - \varepsilon$ formulation, depending on the local distance from the wall: the former is employed in those zones closest to solid walls ensuring better precision, while the latter is used in the free-stream, avoiding the common $k - \omega$ excessive sensitivity to inlet free-stream boundary conditions. This is possible thanks to "blending functions" (based on the computation of local distance from the wall), defined and calibrated to allow the model to automatically work without user input [33].

A complete description of the shear-stress transport (SST) formulation can be found in [43]. Basically, Menter highlighted the importance to take into account in the closure equations the effects of the transport of the turbulent shear stress, $\overline{\rho u'_i u'_j}$, since this is the main factor limiting standard Eddy-Viscosity models (but not Reynolds Stress Models). The eddy viscosity is then modelled via:

$$\mu_T = \frac{\rho a_1 k}{\max(a_1 \omega, \Omega F_2)} \quad (2.28)$$

where $a_1 = 0.31$, Ω is the absolute value of vorticity and F_2 is one of the mentioned blending functions. The denominator of the previous equation implicitly states that no damping is required in the SST model, since either laminar or viscous stresses is used to compute μ_T depending in the distance from the wall.

The SST formulation is recognized to behave well in presence of adverse pressure gradients and separating flows. Also, it limits the overestimation of turbulence energy production in highly sheared flows (e.g. around stagnation points, impinging jets), which is common to every Eddy-Viscosity model since they rely on the isotropic turbulence assumption.

In the OpenFOAM framework, the $k - \omega$ SST is the only one allowing the use of scalable wall functions. Scalable wall functions virtually displace the mesh to a $y^+ \approx 11.126$, irrespective of the level of near-wall grid refinement. This value of y^+ marks the intersection of the linear and logarithmic velocity profiles, thereby the erroneous modelling of the laminar sub-layer and buffer region is avoided whatever the local value of y^+ is. The result should be a continuous profile of properties all the way to the solid wall [21].

2.2.3 Higher accuracy CFD

LES

Large eddy simulations are a mathematical model for turbulence firstly proposed by Smagorinsky [46]. LES is meant to avoid the resolution of the entire range of turbulent phenomena via low-pass filtering of the Navier-Stokes equations. Such a filtering can be viewed as a time and spatial averaging removing small-scale information from the numerical solution: the result is a direct simulation of 80% to 90% of the turbulent energy spectra.

LES is recognized to perform well in a variety of engineering problems, providing access to instantaneous turbulence informations. It is also known to be much more computationally expensive if compared to RANS simulations, since a ~ 30 times mesh is needed (this also drops the maximum time step ensuring numerical stability).

DNS

Direct numerical simulations actually do not need any turbulence model or filtering, since the Navier-Stokes equations are resolved taking into account the whole range of spatial and temporal turbulent scales. DNS is claimed to be a research tool rather than a solver for engineering problems; this is due to its extremely high computational cost, which also increases exponentially with the Reynolds number of the simulated flow field.

Chapter 3

Experimental Investigation with LITGS

In this Chapter, the application of the Laser Induced Thermal Grating Spectroscopy (LITGS) technique to time-resolve the passage of synthetic compositional spots in a simplified set up, based on the Cambridge Wave Generator, is presented. Results are part of the work by De Domenico *et al.* [12].

The aim of the present experiment is to assess if LITGS may be used to obtain instantaneous, high frequency measurements of unsteady density variations in a compact experimental set-up, requiring only limited optical access.

3.1 Overview of the technique

LITGS is a laser diagnostic technique generally used to obtain quantitative temperature measurements at the crossing point of two equally polarized pump laser beams from the same pulsed source. Those beams are crossed at an angle θ_p to create the probe volume, where they generate an interference grating pattern of spacing Λ determined by the crossing angle and the laser wavelength, λ (see Fig. 3.1).

$$\Lambda = \frac{\lambda}{2 \sin \frac{\theta_p}{2}} \quad (3.1)$$

The interaction between the interference region and the medium leads to two simultaneous processes that compete against each other: a non-resonant process (forming the electrostrictive grating used for LIEGS) [10] and a resonant process, forming the thermal grating used for LITGS. The former process is not discussed here: it generally produces signals being several order of magnitudes lower than the thermal signals (in presence of an absorbing species), and requires at least a ten times higher pump laser energy.

If λ corresponds to the wavelength for molecular excitation of a species of interest, or that of a seeder, electronic transition occurs: the species is excited and the absorbed energy is released in a few nanoseconds by collisional quenching processes, leading to localized heating. The local gas expansion produces a stationary density perturbation across the interacting region, which causes an acoustic wave to be generated and propagated through it. The situation leads (within a hundred of nanoseconds) to an interference between a stationary and a propagating wave which can be detected using a probe beam; this is introduced in the interaction region at the Bragg angle, θ_B , and its refraction is captured as the LITGS signal.

$$\theta_B = \sin^{-1} \frac{\lambda}{2\Lambda} \quad (3.2)$$

Since the propagating wave moves at the local speed of sound, c , the modulation of the scattered signal appears at a frequency determined as:

$$f = \frac{c}{\Lambda} \quad (3.3)$$

Assuming an ideal gas equation of state, f can be used to determine the local properties of the flow:

$$c^2 = (f\Lambda)^2 = \frac{\gamma \mathcal{R} T}{W} = \frac{\gamma p}{\rho} \quad (3.4)$$

where γ is the ratio of specific heats, \mathcal{R} the universal gas constant, W the mixture molecular mass, and p , T , ρ are the local flow properties.

Once the thermodynamic properties of the flow are known, Equation 3.4 allows to relate the signal frequency to local changes in pressure, temperature or density. Conversely, when the mixture is at constant temperature and pressure, the local molar fraction in a binary mixture can be determined since it is related to the variation of thermodynamic properties. In this work, LITGS has been employed to probe the second typology of flow fluctuations.

In the present configuration, described in details in the next section, a PIV pump laser is employed: it allowed to perform high frequency (500 Hz) measurements, employing low energy pulses (0.5 mJ). However, its characteristic wavelength of 355 nm forced the use of biacetyl to seed the flow, since this is the only semi-harmless volatile substance which absorbs the 355 nm wavelength to generate the thermal grating.

Since LITGS is based on the generation of a local density change by absorption of energy provided by the pulsating laser, it is a slightly intrusive technique. The intrusiveness is low as long as both the pump beam energy and the concentration of the absorber are kept low [12]; on the other hand, those also need to be sufficiently high in order to provide a detectable LITGS signal and a reasonable accuracy in the determination of the signal frequency, f .

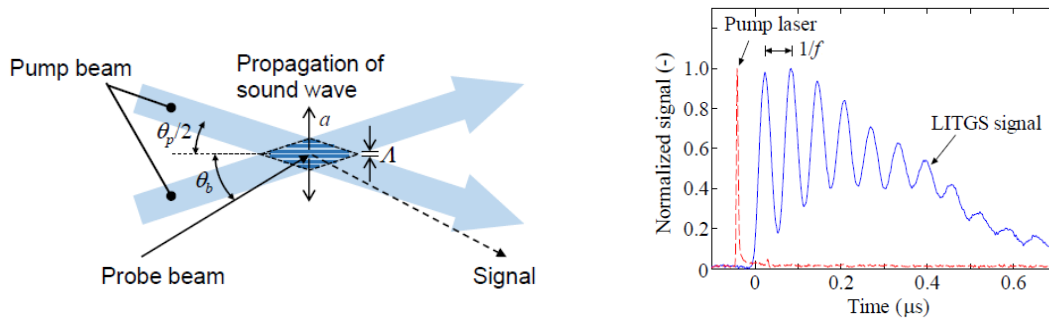


Fig. 3.1 LITGS technique. Left: schematic view of the interference grating pattern. Right: example of a typical LITGS signal produced by a single pump laser shot [52].

3.2 Experimental set-up

3.2.1 Optics

The optical layout is sketched in Fig. 3.2. It is composed by [12]:

- a Edgewave IS200-2-L laser, which generates the the pulsed laser beams producing the thermal grating. It has a wavelength $\lambda = 355$ nm and delivers approximately 0.5 mJ per pulse with a frequency of 0.5 kHz;
- a 50/50 beam splitter, dividing the pump beam into two identical beams (separated by 12 mm);
- a 8 mm thick quartz plate, to compensate the optical delay between the two beams;
- a 300 mm focal length focusing lens, with a crossing angle $\theta_p \approx 2.3$ deg;
- a photodiode (DET210) pointing where one of the two pump laser beams is dumped, to provide the trigger signal;
- a CNI MML-671 diode-pumped solid state laser, producing the continuous probe beam (wavelength = 671 mm, power = 300 mW, diameter ≈ 1 mm);
- a 99:1 splitter, used to split and acquire the continuous probe beam after correcting the alignment;
- a Hamamatsu photomultiplier (H6780-20), used to detect the scattered beam;
- a 4 channels LeCroy 6104A oscilloscope (1 GHz bandwidth, sampling rate 10 Gs/s, 40 million points maximum real time memory), sampling a period of $1 \mu\text{s}$ (10000 points) for every laser pulse.

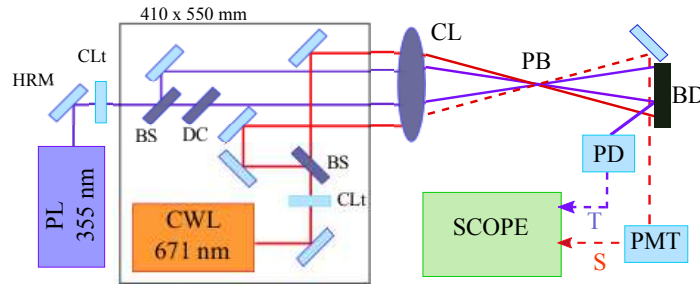


Fig. 3.2 Optical layout [12]. PL: 355 nm pulsed pump laser; CWL: 671 nm continuous solid state laser; PD: photodiode; PMT: photomultiplier; HRM: reflective mirror; BS: beam splitter; BD: beam dumper; CL: crossing lens; CLt: convex lens telescope; DC: delay compensator; S: signal; T: trigger.

3.2.2 Experimental layout

The passage of compositional spots is detected in the configuration represented in Fig. 3.3 [12]. The main flow consists of filtered air controlled by a 250 slpm Alicat mass flow controller ($\pm 0.8\%$ accuracy, $\pm 1\%$ full scale); the flow is seeded with biacetyl (2,3-Butanedione; 99%; Acros Organics CAS: 431-03-8) using a Dresheld bottle bubbler with sintered heads, kept at ambient temperature. The seeded air supply line is connected to the duct inlet via a 8 mm internal diameter, 1.5 meter long plastic tube.

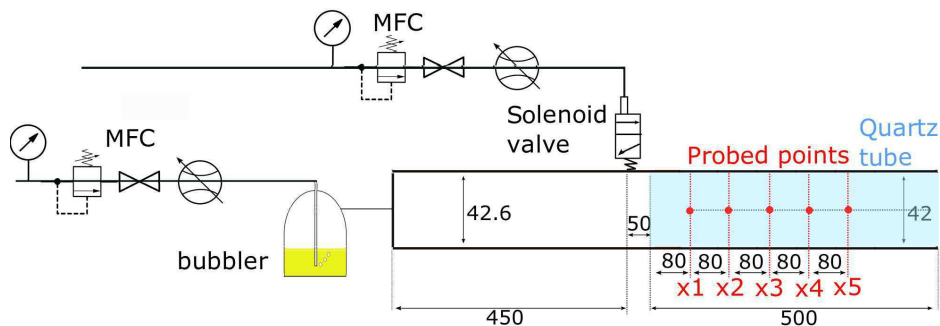


Fig. 3.3 Experimental layout: representation of the Entropy Wave Generator with optical access provided by the quartz tube, including the sampled points locations. Dimensions in millimeters, not to scale [12].

The duct is divided in two parts, clamped together by metal flanges. The first part consists of a PVC tube (42.6 mm internal diameter, 500 mm long), which houses the inlet of the secondary gas, placed 450 mm downstream of the duct inlet; the secondary flow is pulsed by a fast response solenoid valve (ASCO Numantics HSM2L7H50V), which is connected to the main duct via a 5 mm internal diameter, 200 mm long plastic tube and a 4.8 internal diameter, 30 mm long metal flange. The latter part of the rig consists of a 500 mm long, 42

inner diameter UV grade fused silica tube (wall thickness of 2 mm), the downstream end of which is left open to the atmosphere; the quartz tube provides optical access, and the LITGS probe signal is aligned to the centreline of the duct, sampling at the five axial location reported in Fig. 3.3.

3.3 Detection of unsteady compositional spots

3.3.1 Procedure

An investigation of the trade off between intrusiveness and precision has been carried out by De Domenico *et al.*, since changes in the air flow properties (temperature, specific heat and molar mass fraction) caused by the seeder and the laser pulse should be taken into account when the LITGS frequency is determined. The expected frequency can be expressed rewriting Equation 3.4 as a function of the biacetyl concentration, X_b , and the expected local temperature rise:

$$f^2 = \frac{1}{\Lambda^2} \frac{\gamma \mathcal{R} T}{W} = \frac{1}{\Lambda^2} \frac{\left(1 - \frac{\mathcal{R}}{c_{p,a}(1-X_b) + c_{p,b}X_b}\right)^{-1} \mathcal{R}}{W_a(1-X_b) + W_b X_b} (T_a + \Delta T) \quad (3.5)$$

where the specific heat, c_p , of air and biacetyl (subscript a and b respectively) are assumed to be constant with temperature and reported in Table 3.1, together with the respective molar mass, W .

Table 3.1 Properties of air and biacetyl.

	Molar mass, W [g mol ⁻¹]	Specific heat, c_p [J mol ⁻¹ K ⁻¹]
Air	28.971	29.115
Biacetyl	86.09	120.97

The employed optical set-up produces a grating of spacing 8.7 μm in a probe volume having estimated length of ~ 30 mm and width and height of ~ 1 mm. In combination with the low pulse energy of the PIV laser, this can be verified to produce a negligible thermalisation effect on f , so the ΔT term in Equation 3.3.1 is neglected.

Composition spots are generated by radial injection of helium, carbon dioxide and argon, and their convection and dispersion is investigated downstream. The mass flow rate of air is set to 1.57 g/s, producing a Reynolds number Re_D (based on the PVC duct diameter, $D = 42.6$ mm) equal to ~ 2570 . This value was limited by the consumption rate of biacetyl

and the bubbler volume: in fact, as shown by De Domenico *et al.*, high seeder concentrations should be used in order to obtain high signal to noise ratios in the LITGS signal; on the other hand, this implies changes in properties of the measured flow that must be taken into account to assess higher precision. The procedure developed by De Domenico *et al.* to take into account the presence of the seeder when evaluating the base flow LITGS frequency (f_0) is explained in details in [12]. When the bubbler is filled of biacetyl the maximum seeder amount is delivered, resulting in an estimated biacetyl concentration $X_b \approx 0.03$. It should be noted that such a value generates an estimated shift of the main flow frequency, f_0 , approximately equal to 3.8% if compared to the value expected if no seeder was used. However, an error in the evaluation of the biacetyl concentration of $\Delta X_b = 0.01$ (i.e. about 30% of the expected value) would lead to an error in the density change due to the injected gas $\Delta\rho/\rho_0 < 1\%$, thus the quantitative results presented in the next section are reliable.

Signals are acquired at 10 Gs/s on a 1 μ s time window, and discretized in 10000 points. The raw voltage signal is padded with zeros up to 2^{19} points, producing a signal approximately 52 times longer, prior to applying the Fast Fourier Transform. Under this conditions, the LITGS frequency for the steady main flow, f_0 , is acquired at each probe location: signals have an average amplitude of 200 mV, and 1000 shots are sampled. This produces a standard deviation to base flow frequency ratio of 1%.

Once f_0 is determined, the different gases (He, CO₂, Ar) are injected with a frequency of 1 Hz and a duty cycle of 20%. At each probed point, the passage of 30 consecutive spots was recorded in order to produce phase-averaged traces. The sampling frequency, determined by the laser pulses, is 0.5 kHz. At every laser shot the LITGS frequency signal, f , is acquired. Figure 3.4 summarize the fundamental post-processing steps, referring to the first probe location (x_1 in Fig. 3.3): it reports the time resolved peak frequency of the LITGS signal and the following ensemble-averaged trace in terms of frequency variation from the mean flow.

Remembering Equation 3.4 (in which Λ is a geometric constant) and assuming constant temperature and specific heats of the species, f can be expressed only in function of mean flow properties (already corrected considering the presence of the seeder) and the molar mass fraction of the injected gas, X_i :

$$\left(\frac{f}{f_0}\right)^2 = \frac{\left(1 - \frac{\mathcal{R}}{c_{p,i}X_i + c_{p,0}(1-X_i)}\right)^{-1}}{\left(1 - \frac{\mathcal{R}}{c_{p,0}}\right)^{-1}} \frac{W_0}{W_i X_i + W_0(1 - X_i)} \quad (3.6)$$

from which X_i is extracted. The density variation in the base flow caused by the compositional spot is then computed as:

$$\frac{\Delta\rho}{\rho_0} = \frac{\Delta W}{W_0} = \frac{W_i X_i + W_0(1 - X_i)}{W_0} - 1 \quad (3.7)$$

while the secondary gas mass fraction is simply given by:

$$Y_i = \frac{X_i W_i}{X_i W_i + (1 - X_i) W_0} \quad (3.8)$$

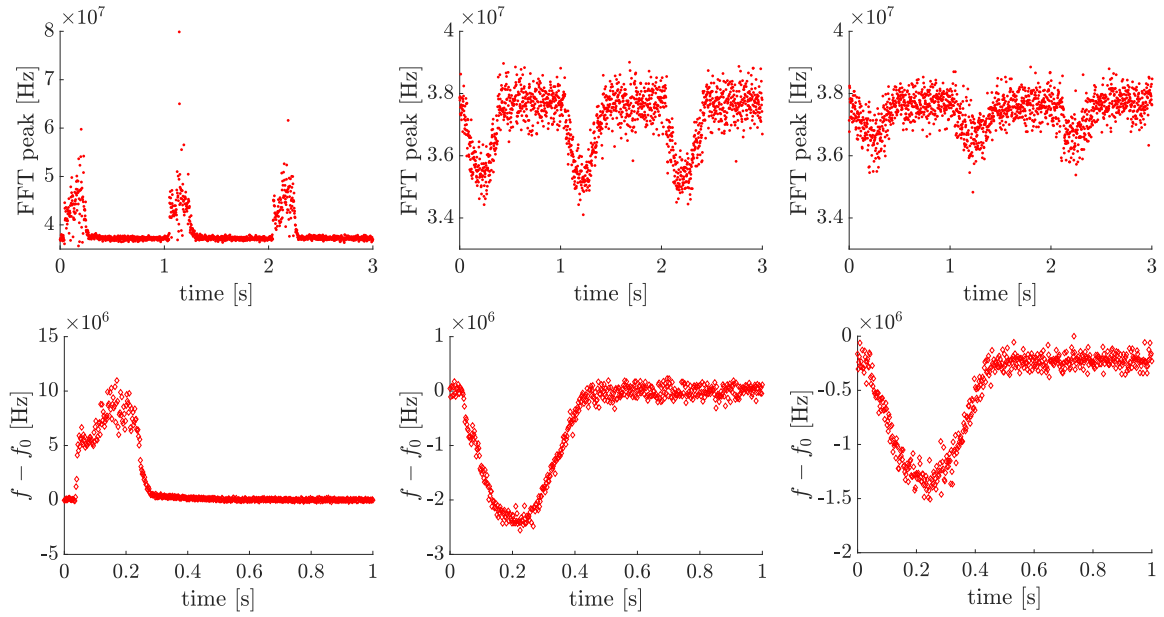


Fig. 3.4 Post-processing steps (from left to right: He, CO₂, Ar), at the first probed point x_1 . Top: time resolved LITGS traces (peak frequency) for 3 pulses. Bottom: ensemble-averaged (30 pulses) LITGS signals (frequency variation from that of the mean flow).

3.3.2 Results

Averaged traces of the secondary gas mass fraction and normalized density variation are reported in Fig. 3.5.

The passage of each compositional wave is successfully detected, and slight diffusion effects can be seen despite the short convective length. The helium traces show a more relevant noise because the speed of sound (and so the signal frequency) is much higher than for the CO₂ or Ar cases and, as the quenching efficiency is lower, the LITGS signal has lower amplitude and duration, so the determination of f after the passage of a helium spot is affected by larger error.

The previous problematic has been clarified by De Domenico *et al.* [12], detecting the LITGS signals provided by pure steady jets of air, carbon dioxide, argon and helium

seeded by biacetyl. Figure 3.6 shows the ensemble-averaged (1000 shots) signals for the different gases, as function of time and in the frequency domain: in this configuration, only two peaks could be observed in the helium signal, so the corresponding frequency could not be extracted from the frequency spectrum.

Another source of noise in the traces of Fig. 3.5 is the consumption rate of the seeder during the acquisition of consecutive spots. This causes the vaporisation of biacetyl to become less efficient, so a slight shift in the base flow frequency, f_0 may occur.

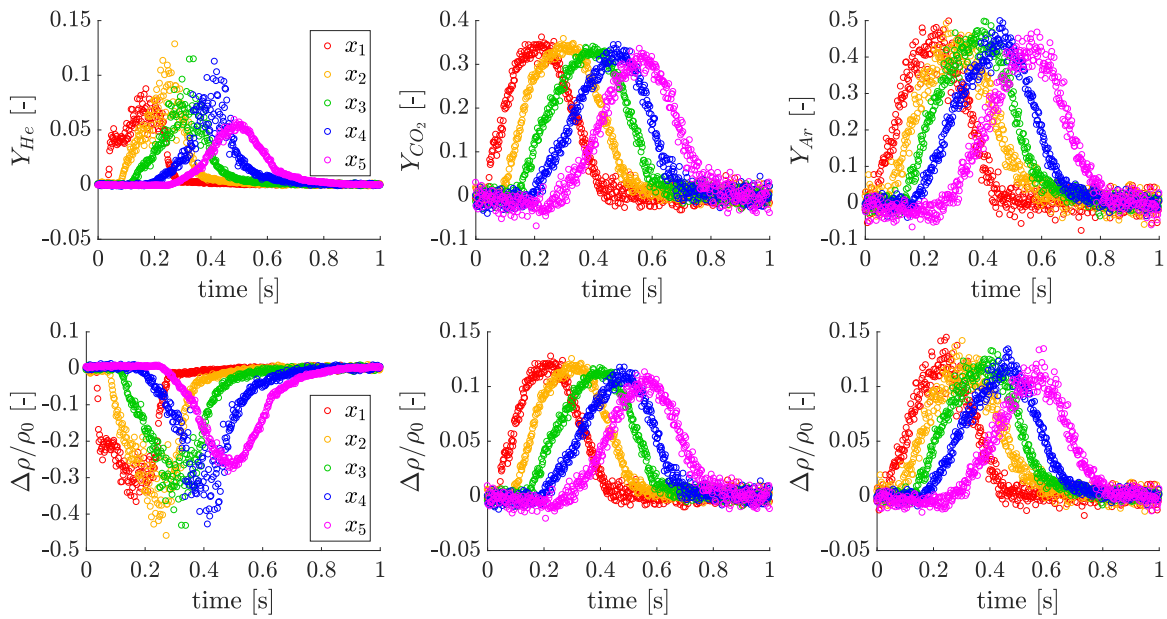


Fig. 3.5 Detection of compositional spots (from left to right: He, CO₂, Ar). Ensemble-averaged secondary gas mass fraction (top) and normalized density variations (bottom), at five axial locations along the quartz tube center line.

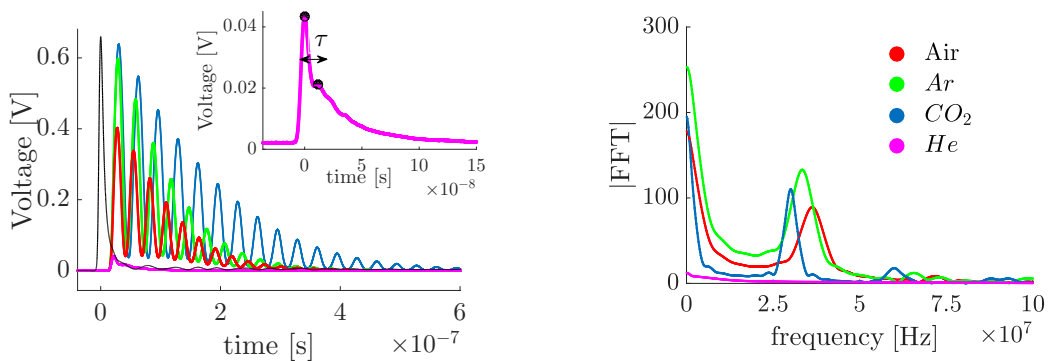


Fig. 3.6 LITGS signals acquired in a steady jet of biacetyl-saturated air, CO₂, Ar and He. Right: ensemble-averaged signals; inset: zoom on helium signal. Left: corresponding Fourier transform of the signals [12].

3.4 Determination of boundary conditions for simulations

Because of the extremely fast changes of flow conditions in the secondary gas line when the valve is triggered, the mass flow controller did not provide a reliable estimation of the injected mass flow which generates the compositional spots (\dot{m}_i). Thus, the phase averaged mass fraction traces of each gas (Fig. 3.5) are used to provide an estimation of this value, that will be used as boundary condition in the CFD simulations presented in Chapter 4. Specifically, \dot{m}_i is derived a posteriori from the peak value in the mass fraction signal at the first probed location, according to:

$$\dot{m}_i = \frac{[\max(Y_i)]_{x_1}}{1 - [\max(Y_i)]_{x_1}} \dot{m}_{air} \quad (3.9)$$

This is justified by the fact that experimental data do not show a relevant dispersion of the compositional wave travelling downstream, so the procedure is assumed valid to assess if the simulations (and, specifically, OpenFOAM's solvers) are providing a reliable prediction of the convection-diffusion process.

Therefore, the inlet boundary conditions used in Chapter 4 to simulate the present LITGS experiments are:

Table 3.2 Estimation of the injected mass flow for each gas, used as inlet boundary condition in the simulations.

Injected mass flow, \dot{m}_i	
[g s ⁻¹]	
He	0.136
CO ₂	0.704
Ar	1.19

Chapter 4

Numerical Simulations

This chapter describes the methods used to model the unsteady propagation of compositional spots, as studied with LITGS experiments in Chapter 3.

4.1 Solvers

CFD simulations were run using the open-source package OpenFOAM 4.1. It is a framework for developing executable applications based on a collection of approximately 100 C++ libraries. OpenFOAM is shipped with about 250 pre-built applications that fall into two categories: solvers, designed to solve the governing equations of a wide range of problems in fluid mechanics, and utilities, that are designed to perform tasks that involve pre-processing and data manipulation [21].

The numerical procedure adopted in the present work was broken into three steps (as described in §4.4) and two solvers from the OpenFOAM suit have been employed:

- *rhoSimpleFoam*: to obtain the steady state solution of the main flow of air before the injection
- *reactingFoam*: to study the unsteady propagation of the compositional spots.

4.1.1 Steady simulations: *rhoSimpleFoam*

The solver *rhoSimpleFoam* is suitable for both laminar and turbulent steady simulations of single-phase, single-species, compressible fluids. It employs the pressure-based (predictor-corrector) approach and the SIMPLE algorithm.

Since only the steady-state solution for the main flow is of interest, relaxation factors have been used to control the change of variables at each iteration, ensuring that no numerical

instabilities occurred. At each iteration n , a new value for variable ϕ is calculated in each cell P ; it is then corrected applying a relaxation factor α as shown in Table 4.1, according to Equation 4.1.

$$\phi_P^{n+1,used} = \phi_P^n + \alpha(\phi_P^{n+1,computed} - \phi_P^n) \quad (4.1)$$

Table 4.1 Relaxation factor used running the steady state simulations with *rhoSimpleFoam*.

Field	Value
p	0.3
ρ	0.5
Equation	Value
\mathbf{u}	0.7
$k-\omega$	0.5
e	0.5

The numerical schemes used to discretise the governing equations for the steady simulations are reported in Appendix A.

4.1.2 Unsteady simulations: *reactingFoam* and modified-*reactingFoam*

The application *reactingFoam* is a transient solver for laminar and turbulent compressible gases involving combustion and chemical reactions. It has been selected since it is the only solver in the OpenFOAM library allowing to solve single-phase but multi-species problems. Since the aim of the present work is to investigate the behaviour of inert species, the solver has been modified in order to switch the reactions off. The solver employs the PIMPLE algorithm, resulting by the coupling of the SIMPLE algorithm and the PISO pressure-velocity loop. In *reactingFoam* the species transport equation is formulated for each species i as follows:

$$\frac{\partial(\rho Y_i)}{\partial t} = -\nabla \cdot (\rho \mathbf{u} Y_i) + \nabla \cdot ((\mu + \mu_{turb}) \nabla Y_i) + \dot{S}_i \quad (4.2)$$

where \dot{S}_i is the source term (equal to zero, since there are no reactions) and μ_{turb} is the turbulent viscosity.

It can be noticed that Equation 4.2 is based on the assumption that the ratio between mass diffusivity and momentum diffusivity is unitary for both the laminar and turbulent term. Thus, the laminar Schmidt number, Sc_{lam} , as well as the turbulent Schmidt number, Sc_{turb} , defined by Equations 4.3, are assumed to be equal to one.

$$Sc_{lam} = \frac{\mu}{\rho D}; \quad Sc_{turb} = \frac{\mu_{turb}}{\rho D_{turb}} \quad (4.3)$$

where D is the mass diffusion coefficient.

It was of interest to investigate how a big role this assumption (implicit in the standard solver) plays in the prediction of the compositional wave convection and diffusion process. To do so, also a modified version of Equation 4.2 has been proposed and used, and results are compared in §4.6; it is formulated as follows:

$$\frac{\partial(\rho Y_i)}{\partial t} = -\nabla \cdot (\rho \mathbf{u} Y_i) + \nabla \cdot ((\mu/Sc_{lam} + \mu_{turb}/Sc_{turb}) \nabla Y_i) + \dot{S}_i \quad (4.4)$$

Equation 4.4 allows the user to set a different value for both the Schmidt numbers (and thus the diffusion coefficients) depending on the gas used to generate the compositional spot. Thermal (Soret) diffusion is not taken into account since the problem is isothermal.

4.2 Thermophysical properties

4.2.1 Transport properties

The modelling of transport properties is needed to solve the energy equation. To do so, the dynamic viscosity, μ , thermal conductivity, k , and thermal diffusivity, α , need to be defined. Since the present simulations deal with an isothermal problem close to the ambient pressure, these properties are assumed to be constant for each species; from those values, the solver can compute the correct value for the mixture, according to the local mass fraction of each species. Therefore, the following values for the dynamic viscosity and the Prandtl number Pr (referred to normal conditions) are implemented [47]:

Table 4.2 Transport properties specified in OpenFOAM solvers.

	μ [kg m ⁻¹ s ⁻¹]	Pr [-]
Air	1.813×10^{-5}	0.705
He	1.960×10^{-5}	0.670
CO ₂	1.469×10^{-5}	0.766
Ar	2.230×10^{-5}	0.680

As mentioned in §4.1.2, also a different species equation is formulated, meant to allow easy modifications to the standard solver *reactingFoam*. As described in the following sections, the injection of each gas has also been simulated implementing values of the

Schmidt numbers different from one; such values are summarized in Table 4.3. The laminar numbers are based on the assumption of binary diffusion coefficients and computed with respect to air according to the Chapman-Enskog theory using the external, free-access tool *Wolfram CDF player* [54]. Turbulent numbers are assumed equal to 0.7, as done in almost every commercial software [48]; the last assumption is also associated with the implementation of a turbulent Prandtl number of 0.7, in order to ensure a unitary turbulent Lewis number [3].

Table 4.3 Laminar and turbulent Schmidt numbers used in the modified-*reactingFoam* for the three gases.

	Sc_{lam} [-]	Sc_{turb} [-]
He	0.220	0.7
CO ₂	1.033	0.7
Ar	0.812	0.7

4.2.2 Thermodynamic properties

A thermodynamic model is required to evaluate the specific heat, c_p , from which other properties can be derived. Since the problem is isothermal, also the specific heat was assumed to be constant for each species; besides, OpenFOAM requires to specify the molecular mass, W , and the latent heat of fusion, H_f [47].

Table 4.4 Thermodynamic properties specified in OpenFOAM for the three gases.

	W [g mol ⁻¹]	H_f [J kmol ⁻¹]	c_p [J kg ⁻¹ K ⁻¹]
Air	28.971	2.54×10^6	1004.5
He	4.0026	2.00×10^6	5190
CO ₂	44.009	8.09×10^6	846
Ar	39.948	1.18×10^6	520

4.2.3 Equation of state

The perfect gas law is implemented:

$$p = \rho \frac{\mathcal{R}}{W} T \quad (4.5)$$

Properties of the mixture (once the secondary gas is injected) are weighted on the local mass fraction.

4.3 Turbulence model

The present work deals with three-dimensional, steady and unsteady simulations involving a variety of Reynolds number values: Specifically, even if the main flow of air has a transitional $Re_D \approx 2570$ (referred to the main duct diameter), the pipe connecting the rig to the air supply causes a local value of ~ 13570 ; further, the secondary gas is expected to produce cross-flow jets having Reynolds numbers ranging from ~ 1840 to ~ 14160 , depending on the case. For these reasons, a turbulence model is required.

The $k - \omega$ SST [51] model has been used, which is the only one in OpenFOAM implementing scalable wall functions. According to the smooth duct theory, the following procedure is adopted to estimate the inlet turbulent properties of the flow. The inlet turbulent kinetic energy, k , is given by:

$$k = \frac{3}{2}(\bar{U}I)^2 \quad (4.6)$$

where \bar{U} is the mean flow velocity at the inlet (given by $\bar{U} = \frac{\dot{m}}{A_{inlet}\rho}$) and I is the turbulence intensity:

$$I = 0.16Re_D^{-1/8} \quad (4.7)$$

The dissipation rate, ε , and dissipation frequency, ω , are respectively determined as:

$$\varepsilon = \frac{c_\mu^{3/4} k^{3/2}}{l} \quad (4.8)$$

$$\omega = \frac{\varepsilon}{k} \quad (4.9)$$

where c_μ is a turbulence parameter typically taken equal to as 0.09, and l is the turbulence length scale; for internal flows, it is assumed that $l = 0.07D$, where D is the inlet diameter.

4.4 Methodology

In this section, the procedure adopted to model the experiments described in Chapter 3 is presented in details.

4.4.1 Steady state simulation of the entire geometry

The first step is to obtain the steady state solution of the velocity field determined by the main flow of air used in the experiments.

4.4.1.1 Model assumptions

The whole duct is modelled according to Fig. 4.1. A structured mesh based on the *multiblock O-grid* strategy has been generated using Ansys ICEM, employing about 1.590 millions of cells. The grid is refined near the walls and the area change, and presents a maximum axial spacing of 2 mm, reduced 0.5 mm near the expansion region; more than 50 cells are used in the radial direction and more than 60 in the azimuthal direction, ensuring a circumferential spacing smaller than 3° .

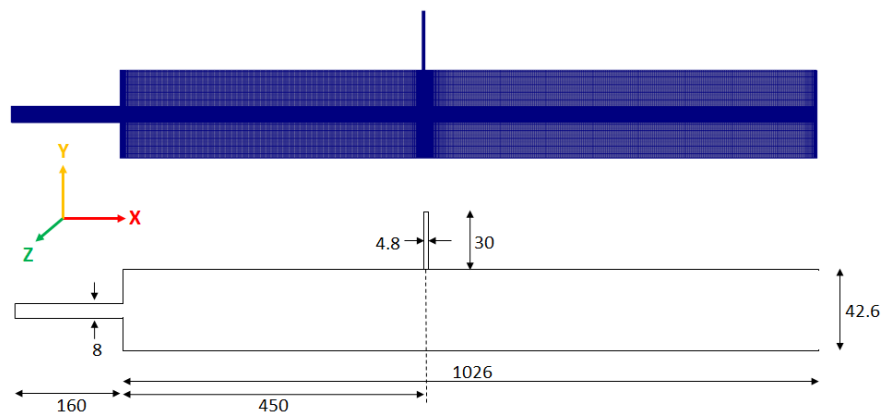


Fig. 4.1 Visualization and sketch of the entire computational geometry (axial length scaled by a factor of 0.33 for clarity). Dimensions in mm.

It should be noted that:

- a longitudinal symmetry plane is adopted to significantly reduce the number of cells. This is acceptable since the injection of the secondary gas is radial and the target of the present work is to study the convection-diffusion of the compositional spot, and not the jet itself;

- the area change due to the use of the quartz duct in the LITGS experiments (having $D = 42$ mm) is neglected; thus, the diameter of the modelled duct is assumed to be constant (42.6 mm);
- the 8 mm diameter pipe connecting the air supply with the duct inlet is modelled in order to obtain a more accurate estimation of the real velocity profile and turbulence properties in the flow field. The modelled length is equal to 160 mm, i.e. twenty times its diameter;
- the radial pipe that will be used for the injection is modelled to represent only the flange connecting the duct with the secondary gas line. Its diameter and length are 4.8 mm and 30 mm, respectively. Since the compositional spot is not injected yet, the radial inlet is now modelled as a wall.

4.4.1.2 Initial and boundary conditions

Boundary conditions used to model the described domain are now reported. Figure 4.2 also provides a graphic representation of their implementation.

Velocity:

- Inlet: a flat velocity profile is implemented by specifying the mass flow entering the domain. Since the target is to simulate the same mass flow of the experiments (1.57 g/s) but a symmetry plan is employed, the value actually set as boundary condition is half the real one.
- Walls: since the present work deals with still bodies, every velocity component at the wall is set to be zero, i.e. $\mathbf{u} = (0, 0, 0)$. This condition is known (and also implemented in OpenFOAM) as *no-slip*.
- Outlet: since the duct is open to the atmosphere and no recirculation is expected, a Neumann boundary condition is used. In OpenFOAM, the *zeroGradient* function allows to specify $\nabla \mathbf{u} \cdot \vec{n} = 0$.
- Symmetry: applied to the velocity, this conditions is equivalent to specify the absence of normal fluxes ($\mathbf{u} \cdot \vec{n} = 0$).

Pressure:

- Inlet: since the inlet velocity has been specified, a *zeroGradient* condition is employed ($\nabla p \cdot \vec{n} = 0$).

- Walls: same as inlet ($\nabla p \cdot \vec{n} = 0$).
- Outlet: since the end is open, an uniform fixed value is used ($p = 1 \text{ atm}$).
- Symmetry: when it comes to scalar properties, the symmetry conditions is equivalent to specify *zeroGradient*; so one has ($\nabla p \cdot \vec{n} = 0$).

Temperature:

- Inlet: air is assumed to enter the duct with a constant static temperature $T_0 = 293\text{K}$.
- Walls: constant static temperature ($T_0 = 293\text{K}$).
- Outlet: *zeroGradient* ($\nabla T \cdot \vec{n} = 0$).
- Symmetry: as for pressure, $\nabla T \cdot \vec{n} = 0$.

Initial and boundary conditions are summarized in Table 4.5.

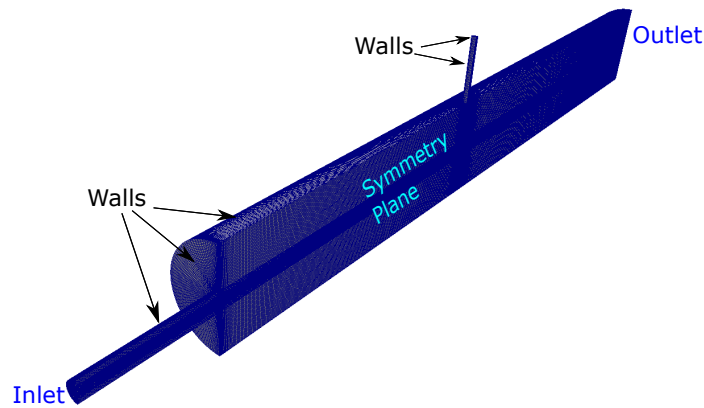


Fig. 4.2 Overview of boundary conditions used performing the steady state simulation of the main air flow in the entire geometry.

Table 4.5 Initial and boundary conditions used for the steady state simulation of the main air flow in the entire geometry.

	Velocity	Pressure	Temperature
Initial field - uniform	$\mathbf{u} = (0, 0, 0)$	$p = 101325 \text{ Pa}$	$T_0 = 293 \text{ K}$
Inlet	$\dot{m}_{air} = 1.57 \text{ g/s}$ - halved	$\nabla p \cdot \vec{n} = 0$	T_0
Outlet	$\nabla \mathbf{u} \cdot \vec{n} = 0$	$p = 101325 \text{ Pa}$	$\nabla T \cdot \vec{n} = 0$
Walls	$\mathbf{u} = (0, 0, 0)$	$\nabla p \cdot \vec{n} = 0$	T_0
Symmetry plane	$\mathbf{u} \cdot \vec{n} = 0$	$\nabla p \cdot \vec{n} = 0$	$\nabla T \cdot \vec{n} = 0$

4.4.1.3 Steady state flow field

The resulting steady state velocity field is reported in Fig. 4.3 in terms of velocity magnitude, with a focus on the expansion region at the inlet of the main duct.

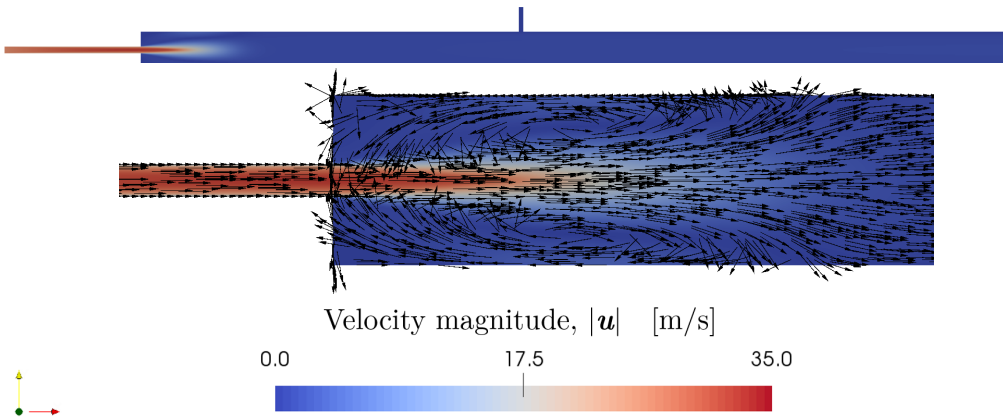


Fig. 4.3 Steady state velocity field (top) and close up of the velocity vectors at the expansion region (bottom) for the entire geometry.

In Fig. 4.4 an overview of the y^+ values at the walls is reported. It clarifies why the $k - \omega$ SST model with scalable wall functions was used: since the mean flow velocity in the main duct is low (~ 1 m/s), employing a mesh to ensure $y^+ > 30$ (as required by standard wall functions) would have led to an extremely coarse wall refinement (7 mm required from the wall to the first node, equivalent to one sixth of the diameter). On the other hand, solving the boundary layer would require at least five cells within $y^+ < 6$ (i.e. in the first millimeter from the wall) leading to an exponential increase in the number of cells, given the high length of the main duct compared to its diameter.

Furthermore, the expansion region at the inlet and the successive radial injection of secondary gas are expected to produce relevant non-uniformities in the y^+ values along the duct wall, leading to a wrong modelling of the near-wall variables by standard wall functions.

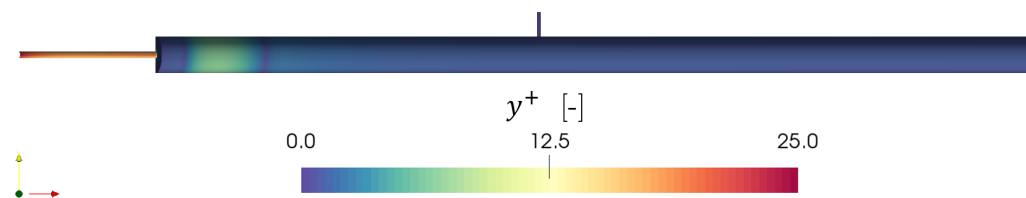


Fig. 4.4 Steady state y^+ values on the walls for the entire geometry.

To verify that the turbulence model is providing realistic results near the walls even working with $y^+ < 6$, a comparison with results by Eggels *et al.* [16] was carried out. A

simulation employing an inlet mass flow $\dot{m}_{air} = 3.308$ g/s was run, in order ensure a duct Reynolds number $Re_D \approx 5400$. The steady state wall velocity profile is sampled 3 cm before the outlet, where a fully developed profile is expected and $y^+ \approx 2$. Figure 4.5 clarifies how the present simulation is correctly modelling the near wall region.

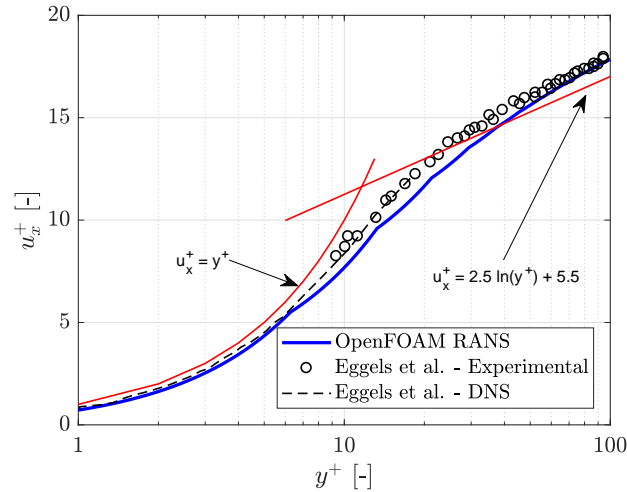


Fig. 4.5 Wall axial velocity profile for a fully developed flow at $Re_D = 5400$: comparison between present OpenFOAM results and data published in [16].

4.4.2 Domain simplification

In order to significantly reduce the computational cost for the unsteady simulations, part of the computational domain upstream of the injection location has been removed. This allows to reduce the number of cells without losing spatial resolution where the compositional spots advection needs to be studied; furthermore, it is possible to generate a more uniform radial distribution of cells near the center line of the duct, since the air supply pipe is removed from the domain.

Figure 4.6 represents the grid used for every unsteady case, where only 10 cm upstream of the injection location are modelled; a grid study was performed for this configuration (see Appendix A). Other dimensions are the same reported in Fig. 4.1, and the symmetry plane is still used. The employed mesh presents a maximum axial spacing of 1.8 mm, reduced to less than 1 mm near the injection location; more than 50 cells are used in the radial direction and more than 70 in the azimuthal direction, ensuring a circumferential spacing smaller than 2.5° .

It is important to ensure that the same flow field is conserved after removing the inlet part of the domain (which produces a recirculation zone, as shown in Fig. 4.3), since this will be initial condition for the mixing process of the secondary gas. To do so, cell values of the

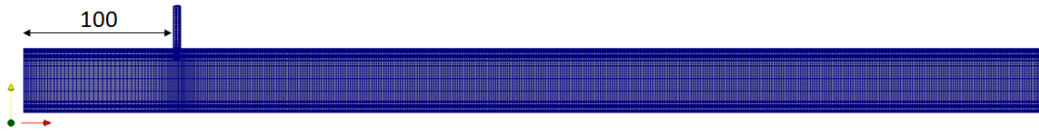


Fig. 4.6 View of the computational grid resulting after the domain reduction. Dimension in mm.

steady state velocity components and turbulence properties (k and ω) have been sampled in the entire geometry solution on a cross section located where the computational domain is cut, i.e. 10 cm upstream of the injection pipe. Those values are then interpolated on the new inlet section of the simplified domain, and used as boundary conditions.

After that, *rhoSimpleFoam* is used to reproduce the steady state flow field in the simplified geometry (Fig. 4.7), which will be the new initial condition for the unsteady simulations. This approach is verified to produce reliable results in Fig. 4.8: it reports the comparison between the axial velocity component and the turbulent kinetic energy, k , at the injection location from the steady state solutions provided by the entire domain and by the simplified one.

The grid adopted to model the simplified geometry gives rise to $y^+ \approx 3$ along the duct when the same mass flow used in the experiments is simulated. Under these conditions, the $k - \omega$ SST model with scalable wall functions has been proved to provide reliable results regarding the near-wall region (see §4.4.1.3). This approach is meant to be easily reused if higher mass flows of air will need to be simulated.

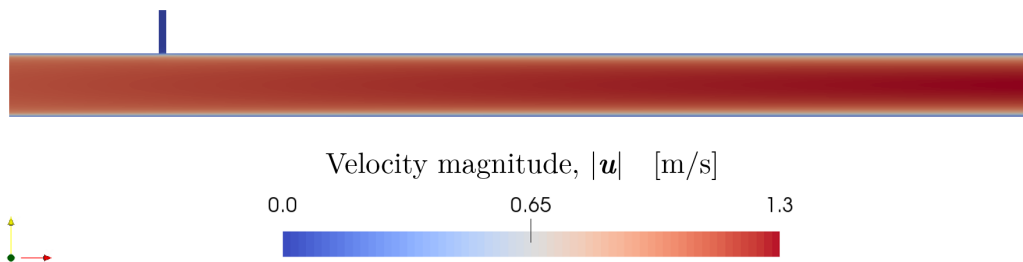


Fig. 4.7 Steady state velocity field for the simplified geometry, using interpolated inlet boundary conditions.

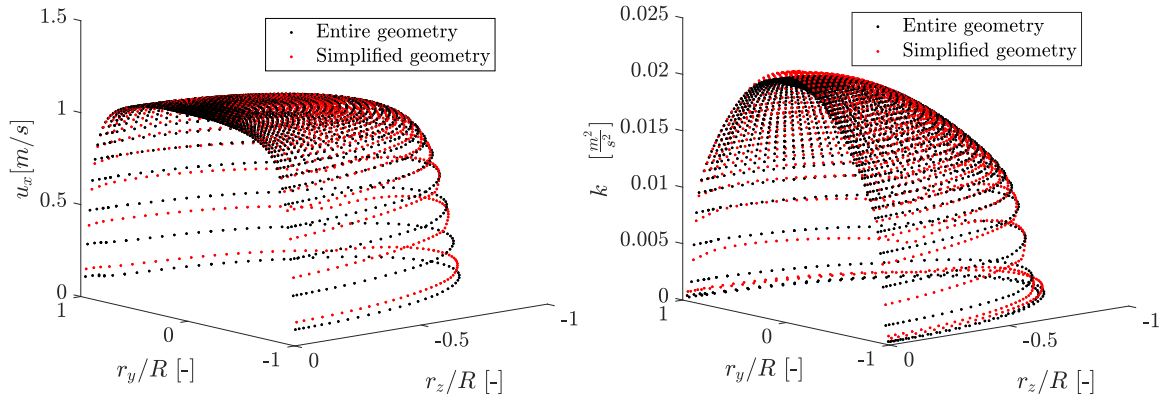


Fig. 4.8 Comparison between the steady state solutions provided by the entire and simplified geometry at the injection location. Right: axial velocity profile. Left: turbulent kinetic energy profile.

4.4.3 Injection process

Using the steady state solution reported in Fig. 4.7 as initial condition, the injection of helium, carbon dioxide and argon is modelled using the standard and modified versions of *reactingFoam*, as presented in §4.1.

4.4.3.1 Cases set-up

For each gas, the total simulated time is equal to one second, where the first 0.2 seconds correspond to the injection duration. A single secondary gas pulse is entirely simulated, in order to allow comparisons with the ensemble-averaged LITGS measurements. Every simulation is performed using a variable time step automatically chosen by the solver in order to ensure a maximum Courant number of 0.59. This allows to maximize the time step as well as to increase it when the injection is over, after which the only relevant phenomenon is the convection of the spot with the low speed mean flow. During the injection period and the convection of the spot, the maximum time steps used by the solver were $\sim 4.5 \times 10^{-6}$ s and $\sim 4.7 \times 10^{-5}$ s respectively, so a good time resolution is ensured.

Boundary conditions used for temperature and pressure are identical to those used for the steady simulations (see Table 4.5). However, the radial inlet is now used to inject the secondary gas, so the velocity boundary condition is modified introducing a second transient mass flow inlet; values obtained a posteriori by LITGS measurements (reported in Table 3.2) are simulated. As done for the air inlet, reference mass flow values are halved since the symmetry plane is employed.

To specify which gas is introduced in the two inlet boundaries, *reactingFoam* requires to set a mass fraction (Y) boundary condition for each patch. Table 4.6 summarizes the modifications done when switching from the steady state case set-up to the transient analysis of compositional spots (the subscript i represents the injected gas).

Table 4.6 Modifications to boundary conditions done before running the unsteady simulations with *reactingFoam*, using the steady state solution as initial condition.

	Velocity	Mass Fraction
Air inlet	Interpolated profile (see §4.4.2)	$Y_{air} = 1$
Gas inlet	$\dot{m}_i = \begin{cases} \text{Table 3.2 - halved} & (0 \text{ s} \leq t \leq 0.2 \text{ s}) \\ 0 \text{ g/s} & (0.2 \text{ s} < t \leq 1 \text{ s}) \end{cases}$	$Y_i = 1$
Outlet	$\nabla \mathbf{u} \cdot \vec{n} = 0$	$\nabla Y \cdot \vec{n} = 0$
Walls	$\mathbf{u} = 0$	$\nabla Y \cdot \vec{n} = 0$
Symmetry plane	$\mathbf{u} \cdot \vec{n} = 0$	$\nabla Y \cdot \vec{n} = 0$

Due to the long period of time that needs to be simulated to obtain a solution comparable with LITGS measurements, there was a clear need for an adequate computational power. For this reason, an account on the University of Cambridge's High Computing Service has been created, specifically to use the Darwin cluster [8]. Every case was run employing two nodes (equivalent to 32 cores), and Table 4.7 reports the computing time required to complete each simulation, including those needed for the two steady state simulations described in §4.4.1 and §4.4.2. It can be observed how the adjustable time step setting (previously described) allowed to keep the required time for each single simulation lower than 12 hours, which is required in order to use a free account service.

Table 4.7 Computing time hours required for each case, running on the Darwin Cluster (32 cores).

Simulation	He	CO ₂	Ar
Steady state - entire geometry	5	5	5
Steady state - simplified geometry	0.5	0.5	0.5
Transient - compositional spot	11	6.2	9.1
Total	16.5 hours	11.7 hours	14.6 hours

4.5 Resulting flow field

As reported in Table 4.6, the injection of compositional spots is simulated by a transient boundary condition for the secondary gas inlet, while the main flow of air is always present. The resulting behaviour of each compositional spot is now reported in terms of secondary gas mass fractions (for CO₂ and Ar) and density variations (for He). Figure 4.9 represents the density variation (non-dimensionalized by the main flow density, ρ_0) induced by the injection of helium. Various time steps are reported, and the injection terminates after 0.2 seconds. Figures 4.10 and 4.11 respectively report the time evolution of CO₂ and Ar mass fraction. The mass fraction for the helium case is not reported since its values are small if compared to those produced by the other two gases; this is due to the low helium molecular mass (one order of magnitude lower than air) and to the injected mass flow, which is more than ten times lower than the main mass flow of air. However, the induced density changes are relevant (nearly 30% downstream of the radial inlet), as clarified by Fig. 4.9.

It can be noticed how each injected gas is predicted to impact on the lower wall of the duct with almost no deviation of its radial trajectory and, as a consequence of the impingement, the generation of wall jets and small recirculation zones is captured. This phenomenon is visualized in Fig. 4.12, which reports the iso-surfaces having $Q = 50000 \text{ 1/s}^2$ coloured by argon mass fraction, for a set of time steps during the injection period. Here it can be observed how the wall vortex expands almost symmetrically during the first 10 milliseconds, with no influence of the main flow of air; after that, the portion of vortex produced downstream gets gradually distorted and convected. At the same time, the upstream part of the vortex seems to reach an equilibrium state with the main flow field during the injection; this can also be noticed in Figures 4.9, 4.10 and 4.11, where the different axial extension of the upstream recirculation zone for the three gases is justified by differences in jet Reynolds numbers: in fact, the injection of helium produces the smallest backward propagating jet since the corresponding jet Reynolds number is ~ 1840 , while for CO₂ and argon it is ~ 12710 and ~ 14160 respectively.

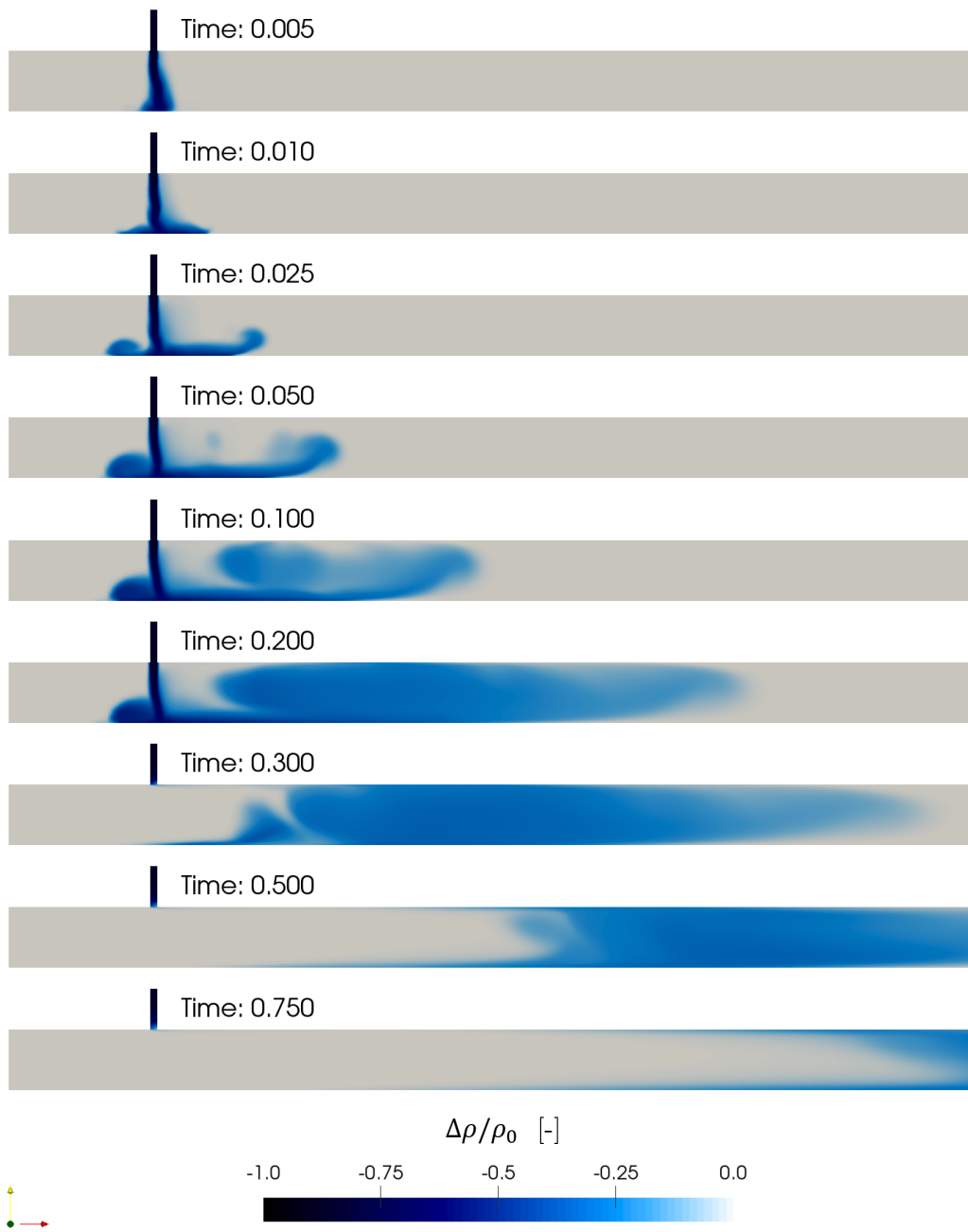


Fig. 4.9 Propagation of helium compositional spot: normalized density variations visualized on the symmetry plane at various time steps (time reported in seconds, 0.2 represents the end of the injection).

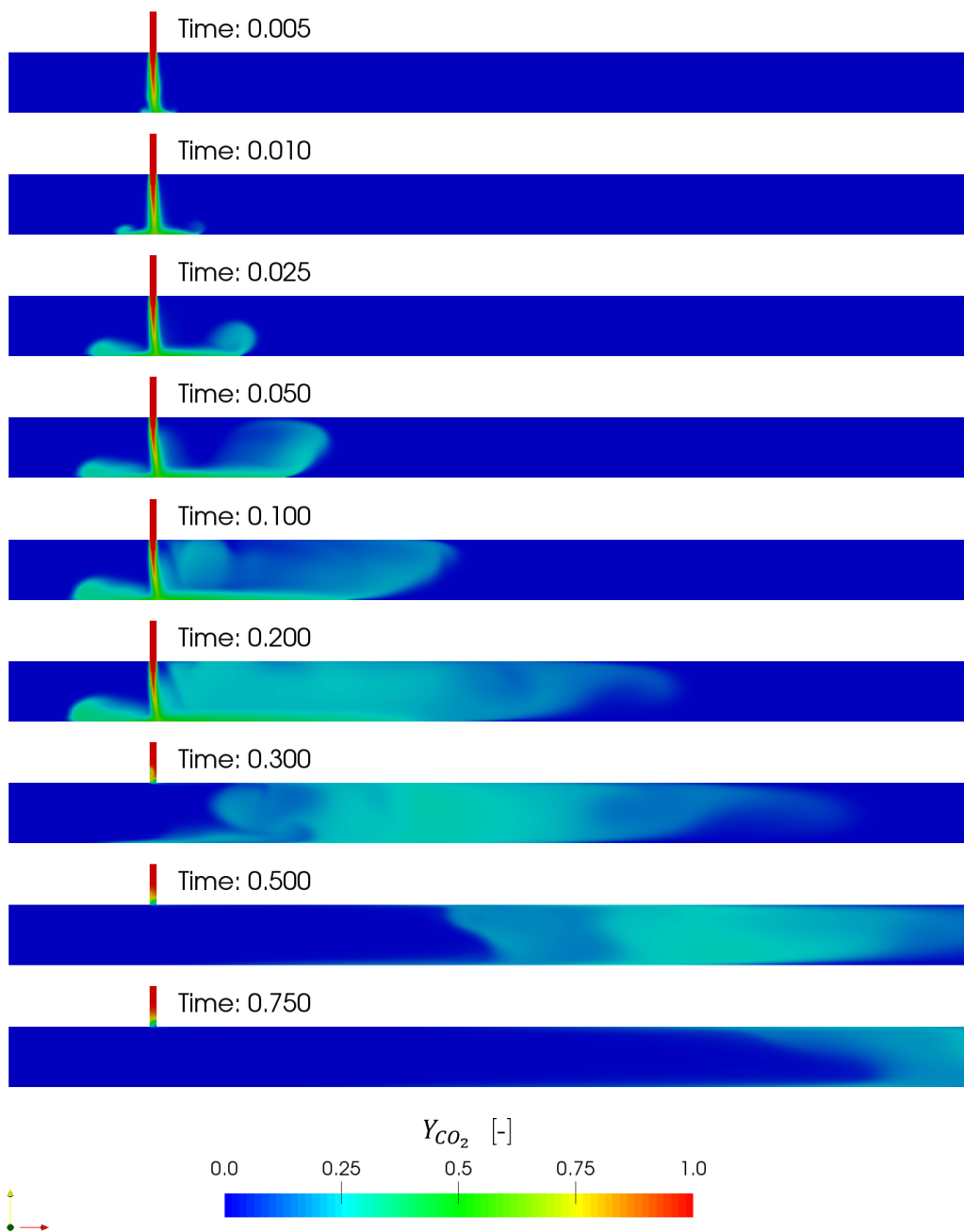


Fig. 4.10 Propagation of carbon dioxide compositional spot: mass fraction of CO_2 visualized on the symmetry plane at various time steps (time reported in seconds, 0.2 represents the end of the injection).

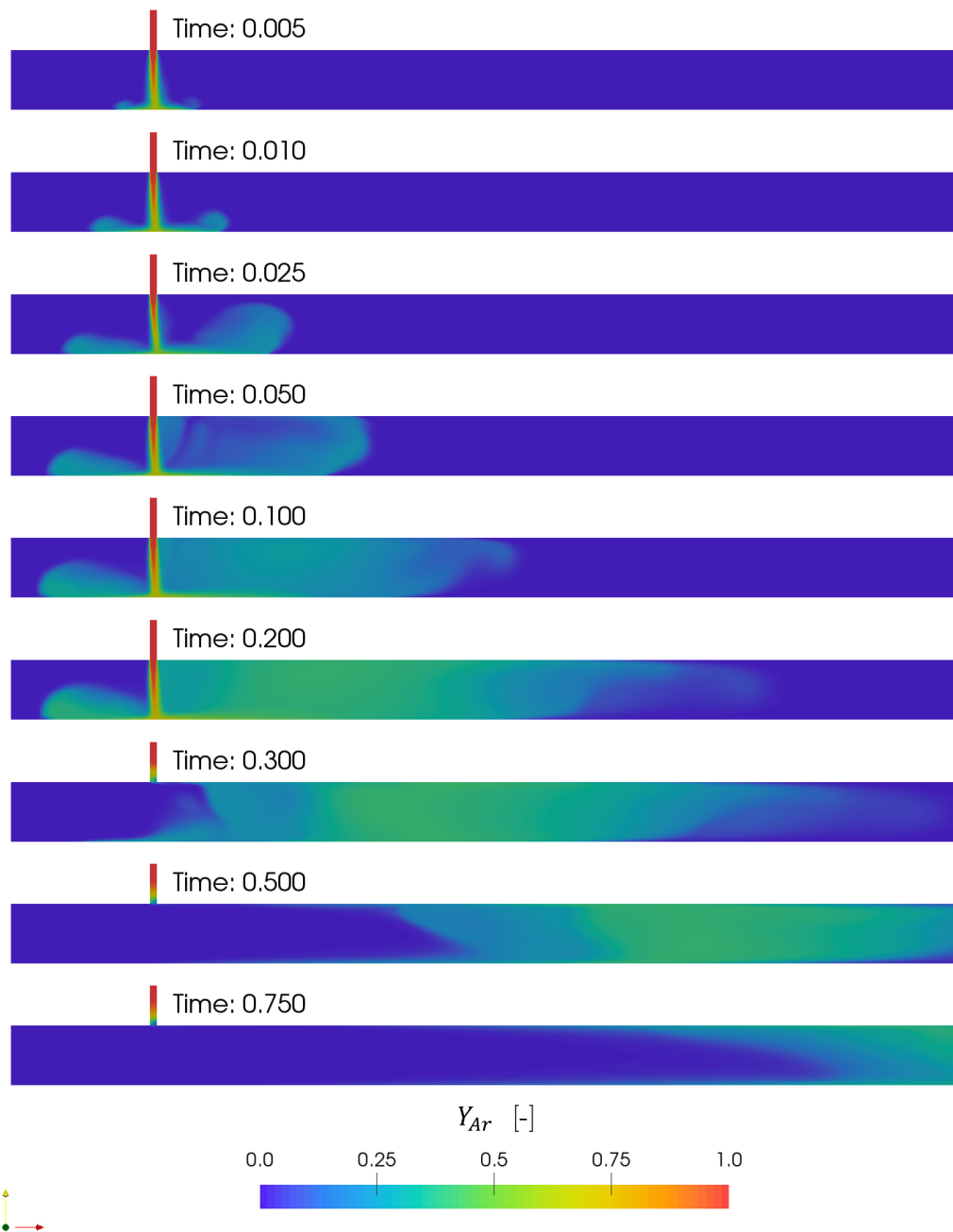


Fig. 4.11 Propagation of argon compositional spot: mass fraction of Ar visualized on the symmetry plane at various time steps (time reported in seconds, 0.2 represents the end of the injection).

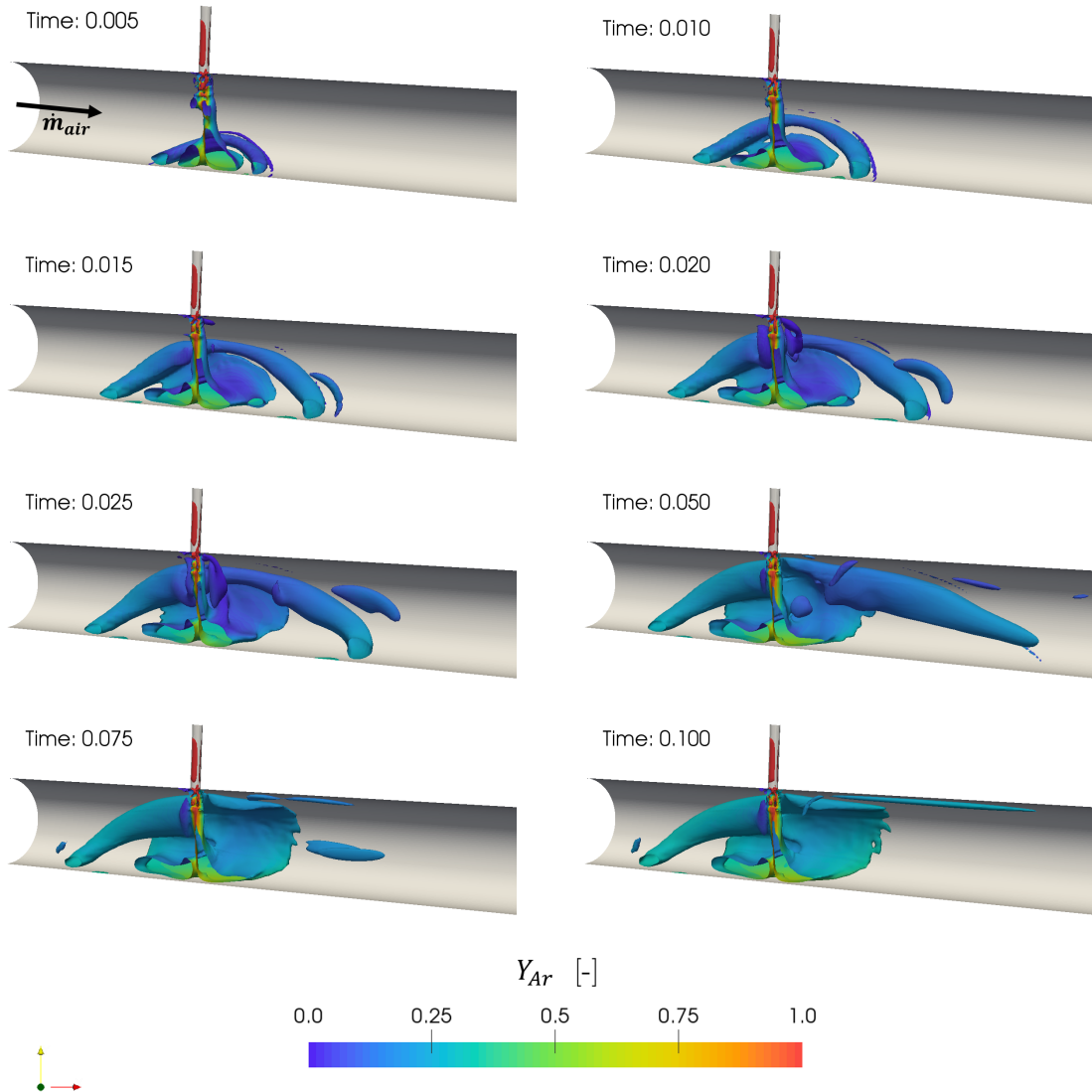


Fig. 4.12 Visualization of wall vortex generation at different time steps in the argon case: iso- Q surfaces¹ ($Q = 50000 \text{ 1/s}^2$) coloured by argon mass fraction. Downstream direction from left to right. Time reported in seconds.

¹Being \mathbf{D} the velocity gradient tensor, defined as $D_{ij} = \frac{\partial u_i}{\partial x_j}$, Q is known to be the its second invariant, e.g:

$$Q = \frac{1}{2}(\text{tr}(\mathbf{D})^2 - \text{tr}(\mathbf{D}^2))$$

Therefore, Q is the balance between the rotation rate and the strain rate; in other words, positive Q iso-surfaces isolate areas where the strength of rotation overcomes the strain, thus making those surfaces eligible as vortex envelopes [23].

4.6 Comparison with LITGS

Mass fractions of the injected gases, Y_i , as well as the mixture density, ρ , have been sampled with a frequency of 1 kHz using punctual probes located on the center line of the duct, at the same axial positions where LITGS measurements were performed. Sampled points are those sketched in Fig. 3.3 as x_1, x_2, x_3, x_4, x_5 , located respectively 13, 21, 29, 37, 45 centimeters downstream of the injection center. A comparison between results provided by the standard and the edited version of *reactingFoam* and experiments is now presented. Results for helium, carbon dioxide and argon are reported in Figures 4.13, 4.14 and 4.15 respectively.

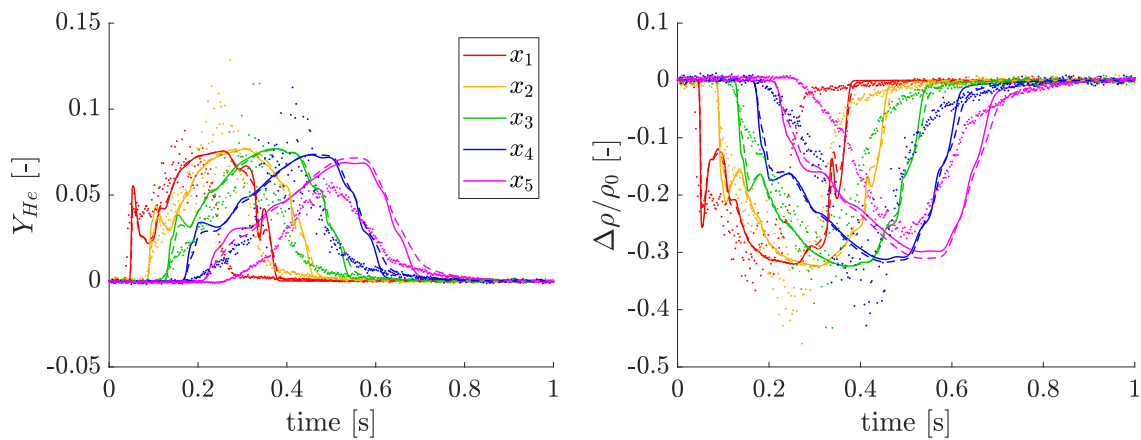


Fig. 4.13 Detection of helium compositional spots at five punctual locations downstream. Left: mass fraction of He. Right: normalized density variations. Time traces provided by the standard solver (—), the modified solver (---) and ensemble-averaged LITGS traces (dots).

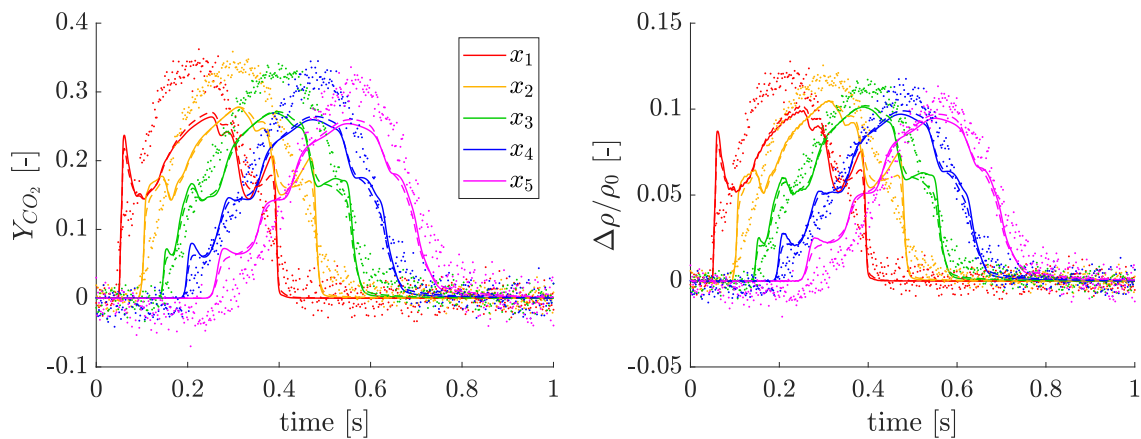


Fig. 4.14 Detection of CO₂ compositional spots at five punctual locations downstream. Left: mass fraction of CO₂. Right: normalized density variations. Time traces provided by the standard solver (—) and the modified solver (---); ensemble-averaged LITGS traces (dots).

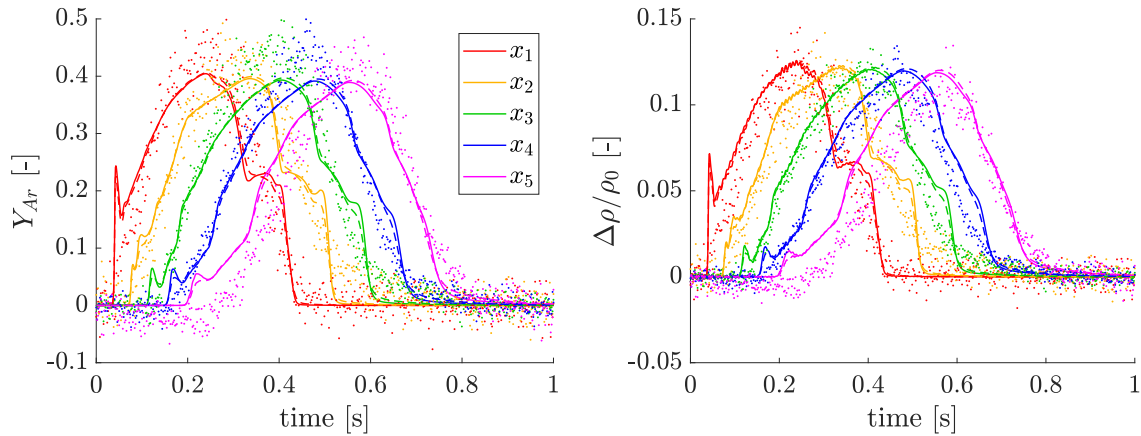


Fig. 4.15 Detection of argon compositional spots at five punctual locations downstream. Left: mass fraction of Ar. Right: normalized density variations. Time traces provided by the standard solver (—) and the modified solver (- - -); ensemble-averaged LITGS traces (dots).

For every injected gas, it can be immediately noticed that differences between predictions by the standard and the modified solver are negligible; only a slight increase in diffusion can be observed in the last probe trace (x_5) for helium, since this is the case with most significant modifications at the species transport equation (Sc_{lam} and Sc_{turb} reduced from 1 to 0.22 and 0.7 respectively). This suggests that neither molecular nor turbulent diffusion are playing an important role in the physics of the problem.

In every case, the wall vortex predicted by the simulations (analysed in Fig. 4.12) causes a local peak in the first probe signal, and its influence can also be observed in the downstream probes signals; this phenomenon is not detected by the experiments, except for its small influence in the first helium trace. One of the influencing factors is surely the turbulence model: since the main flow duct Reynolds number is ~ 2570 , the URANS model may not correctly predict the wall vortex dissipation. A sensitivity study to the employed turbulence model was not performed due to reasons explained in §4.4.1.3. However, it is known how every turbulence model based on the Boussinesq hypothesis leads to overestimation of turbulent kinetic energy in presence of localized impingement or stagnation points, as reported in Chapter 2. A second possible cause for the discussed discrepancy could be the usage of the symmetry condition to model the domain: a more correct prediction of the local wall impingement can be achieved by modelling the entire 3D domain, with obvious consequences regarding computational costs.

Observing the helium case in Fig. 4.13, it can be noticed that the overall amplitude of CFD signals falls within the traces provided by LITGS (except for the last probed point); also, the starting instant of the signal is fairly well predicted by CFD for the first three axial locations. This is an encouraging result given the low absolute values of the sampled mass

fraction. On the other hand, the fourth and fifth signals present a mismatch also in terms of shape if compared to experiments and the peak of each signal is predicted to remain almost constant, even if the width of the density perturbation increases while the spot is convected. Further, simulations provide a nearly constant overestimation of the end instant of each signal (~ 0.1 seconds).

Simulations of CO₂ (Fig. 4.14) resulted in a much better agreement with experiments. The mass fraction is slightly underestimated by CFD at every location, but the agreement in terms of signal shape is encouraging. The main cause for the amplitude mismatch is probably the mass flow of CO₂ used as boundary condition, which is derived a posteriori by experiments as described in §3.4. Mass diffusion of the injected gas is correctly predicted, and so are the starting and final instants of the signals. A more relevant mismatch can be observed for the first probe: this could be caused by the prediction of the impingement of the radial jet, as previously explained.

Finally, the argon case reported in Fig. 4.15 provided a very good agreement with LITGS measurements. It can be observed how amplitude, shape and characteristic times of each signal are correctly predicted by the simulations.

Results obtained with the three different gases clarify what follows:

- Mismatches in signals shape and amplitude for the CO₂ and, especially, helium cases highlight the need for a more accurate boundary condition for the injection: the mass flow absolute value deduced by LITGS data proved to be reasonable, but using a step function profile (0.2 seconds) is surely not representative of the real dynamics of the secondary gas line. A more elaborate inlet condition could be developed by performing local pressure measurements on the rig, to obtain a more realistic prediction of the entering mass flow over time.
- Modifications of the diffusion coefficients did not produce better results, even for the helium case. This suggests that the dissipation of the travelling spot is dominated by shear dispersion. Also, it is likely that further improvements of the species transport equation used in *reactingFoam* (such as the implementation of more complex diffusion models) would not produce relevant changes in results.
- Nevertheless, the OpenFOAM suit and, specifically, *reactingFoam*, has proved to be capable of providing reasonable results for the advection of transient compositional spots; being the solver based on a compressible formulation, its use to predict indirect noise generated by accelerating mass fraction inhomogeneities is a suggested further step.

4.7 Effects of the sampling method

In this section, results provided by the standard solver are examined with the aim of understanding if differences in the spatial sampling method could affect CFD predictions of the compositional wave. For clarity, the following analysis refers only to the standard *reactingFoam* solutions, since no significant differences could be noted if compared to the edited solver (as highlighted in the previous section). This study is meant to investigate if the estimated probing volume of LITGS in the employed configuration could possibly alter the measurements.

Figure 4.16a represents the estimated shape and size of the LITGS grating volume at the center line of the experimental rig: it lies on the horizontal plane, oriented in radial direction (the injection is vertical). Figure 4.16b represents how CFD results are manipulated: the time signals of compositional waves at the five locations along the axis are averaged on 15 mm in radial direction, equal to the half of the estimated grating main dimension (height and width of the LITGS volume are not considered, since they closely match the cell size in the computational grid). A total of 100 equally spaced points is sampled on the radius, and the average on 15 mm comprises 71 of them.

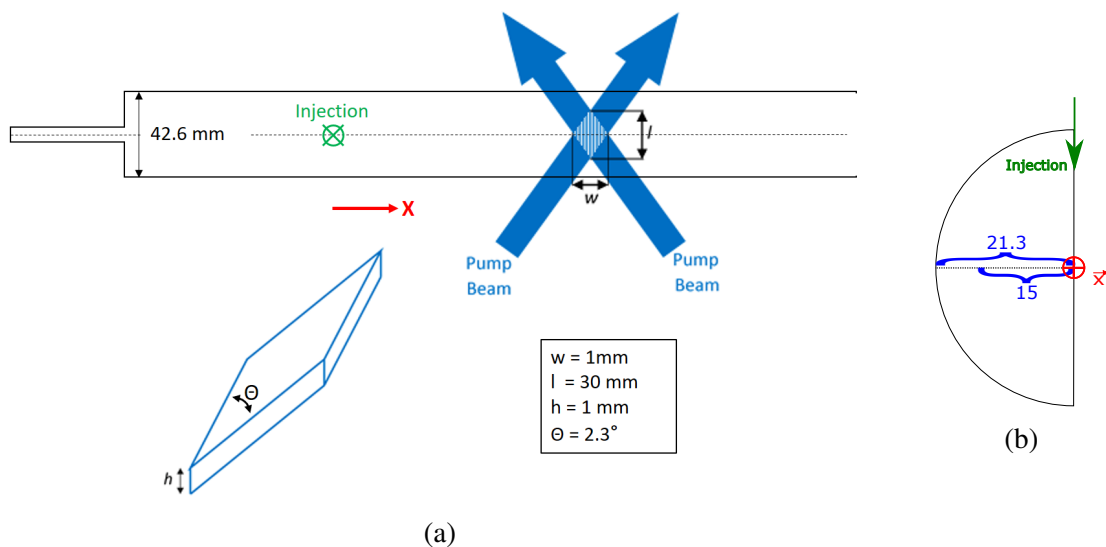


Fig. 4.16 (a): Schematic top view of the experimental set-up, with estimation of the LITGS grating volume; dimensions not to scale. (b): Computational cross section view showing where the averaging is performed; 100 point sampled on the radius. Dimensions in mm.

Further, it was of interest to compare results provided by additional averaging methods, mainly in order to assess if the present configuration could be well approximated to a one-dimensional system: this could be useful with the perspective of exploiting results in

low-order acoustic network codes including dispersion effects. In fact, those models are usually based on one-dimensional formulations, as done by Rolland *et al.* [40].

In summary, the following averaging methods at the five locations along the axis have been used; results are compared in Fig. 4.17, in terms of secondary gas mass fraction over time:

- average in radial direction as sketched in Fig 4.16b. The radius is discretized with 100 points, each one providing a mass fractions value by interpolation of values of the surrounding cells. Mass fractions are then averaged both on 15 mm from the center line, to simulate the LITGS grating main dimension, and on the whole radius. Points are equally weighted;
- area average on the five cross sections of interest, according to:

$$Y_{i,Area-averaged} = \frac{\sum^{N_c} Y_{i,c} A_c}{\sum^{N_c} A_c} \quad (4.10)$$

where N_c is the number of cells (~ 1700) on the considered cross sections;

- mass flow average on the five cross sections of interest, according to:

$$Y_{i,Massflow-averaged} = \frac{\sum^{N_c} Y_{i,c} u_{x,c} \rho_c A_c}{\sum^{N_c} u_{x,c} \rho_c A_c} \quad (4.11)$$

where u_x is the velocity component normal to the considered cross sections.

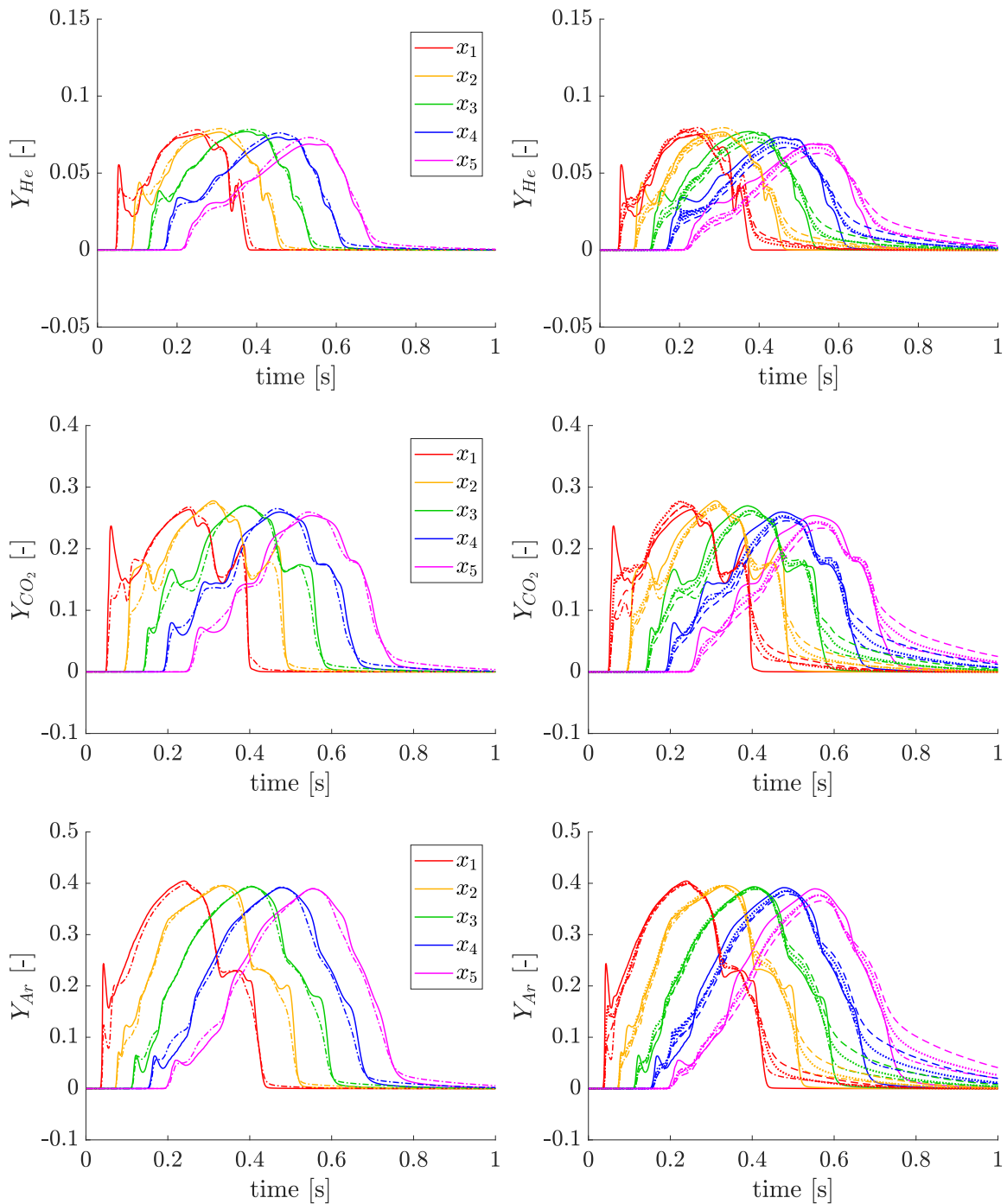


Fig. 4.17 Comparison of sampling methods, standard *reactingFoam*. From the top: He, CO₂, Ar mass fraction over time at five axial locations downstream of the injection.

Left column: punctual probe (—) and average signal on 15 mm along radial direction (---).

Right column: punctual probe (—), average signal on the entire radius (····), area average (- - -) and mass flow average (· · · ·).

Figure 4.17 reports the results for the three injected gases. On the left column, signals from punctual probes are compared to averages on the estimated LITGS grating main dimension: differences can only be observed for the first and second time traces, where the signal peak caused by the jet impingement is significantly reduced, especially for argon and CO₂; the overall trends are not considerably modified. This allows to conclude that, according to the simulations, the actual LITGS probe volume is unlikely to affect measurements. Also, the fact that peaks in the first traces are now smoother provides even better agreement between CFD and experiments (not reported again in the present plot) for argon and CO₂ cases; however, the mismatch in the helium case will not be amended, since the shape of the signal is not significantly modified.

Plots in the right column of Fig. 4.17 compare the punctual CFD time traces to those obtained by averaging on the whole radius length (21.3 mm), by area-averaging and mass-averaging. Generally, every averaging method provides a considerably smoother trace, especially for the He and CO₂ cases, which were showing the most relevant local peaks. Further, the area-averaging predicts the most smooth diffusion of the spots once they are advected: this is expected, since the flow close to the walls (characterized by a large area but small velocity) exerts a higher influence. A similar (but smaller) effect is detected in the mass-averaged trace: because of the strong coupling between density and mass fraction of the gas, this method is actually not as effective for this problem as it was applied to a passive scalar. Finally, the radius average is less affected by high mass fraction values at the walls, so it produces traces closely matching the punctual signals.

This analysis confirms that the dispersion of compositional inhomogeneities in the employed set up is governed by differential convection effects: the present comparisons of averaging methods and results reported in the previous section proved that the molecular and turbulent diffusivity provide a negligible contribute to the wave diffusion if compared to Taylor dispersion effects.

Chapter 5

Low-order modelling

Numerical simulations presented in Chapter 4 proved that neither molecular nor turbulent diffusion are playing a relevant role in the dispersion of the compositional spots. This allows to formulate a simplified theoretical model for the estimation of the wave advection process: this model is based on the convection of the compositional spot in a cylindrical duct, and considers only the shear dispersion mechanism due to the non-uniform velocity profile over the radius [20].

5.1 Formulation

The mean flow is assumed constant over time and purely axial, and effects of the radial injection on the flow field are not taken into account. Thus $\mathbf{u} = (u_x, u_r, u_\theta) = (u_x(r), 0, 0)$.

The transport equation written for the mass fraction of the secondary gas is:

$$\frac{DY_i}{Dt} = 0 \quad (5.1)$$

where $Y_i = Y_i(x, r, t)$ is assumed not dependent on the circumferential coordinate. All the previous assumptions lead to the following simplification:

$$\frac{\partial Y_i}{\partial t} + u_x(r) \frac{\partial Y_i}{\partial x} = 0 \quad (5.2)$$

Applying the Fourier Transform, the mass fraction is now considered in the frequency domain and denoted with a hat: $F[Y_i(x, r, t)] = \hat{Y}_i(x, r, \omega)$. Being j the imaginary unit, one gets:

$$j\omega \hat{Y}_i + u_x(r) \frac{\partial \hat{Y}_i}{\partial x} = 0 \quad (5.3)$$

After performing an integration and assuming as boundary condition a compositional wave which is constant over radius $\hat{Y}_{i,0}(x = x_0, \omega)$, it can be shown that:

$$\hat{Y}_i(x, r, \omega) = \hat{Y}_{i,0} \exp[-j\omega x/u_x(r)] \quad (5.4)$$

Finally, performing the mass flow average on the duct radius, R , the mass fraction is no more dependent on r :

$$\hat{Y}_i(x, \omega) = \hat{Y}_{i,0} \frac{\int_0^R 2\pi r \rho u_x(r) \exp[-j\omega x/u_x(r)] dr}{\int_0^R 2\pi r \rho u_x(r) dr} \quad (5.5)$$

If the density is assumed to be constant, the problem is reduced to the transport of a passive scalar, affected only by shear dispersion. Obviously this hypothesis is not entirely representative of the real problem, but it allows to immediately derive a one-dimensional transfer function, \hat{H} , for the compositional perturbation:

$$\hat{H}(x, \omega) = \frac{\int_0^R r u_x(r) \exp[-j\omega x/u_x(r)] dr}{\int_0^R r u_x(r) dr} \quad (5.6)$$

$$\hat{Y}_i(x, \omega) = \hat{H}(x, \omega) \hat{Y}_{i,0} \quad (5.7)$$

It is also possible to define a second formulation of the transfer function \hat{H} , based on the area average concept instead of the mass flow average. This method is sometimes preferred (as in the work on entropy waves by Morgans *et al.* [34]), so it could be instructive to formulate the following expression:

$$\hat{H}_{area-averaged}(x, \omega) = \frac{\int_0^R 2\pi r \exp[-j\omega x/u_x(r)] dr}{\int_0^R 2\pi r dr} \quad (5.8)$$

5.2 Application to LITGS results

Using as boundary condition, $\hat{Y}_{i,0}$, the signal provided by the first probed point in the LITGS measurements, it is possible to assess if the problem is effectively dominated by Taylor dispersion, and if the present transfer function correctly predicts the amplitude and shape of the traveling wave. The considered velocity profile, $\mathbf{u} = (u_x(r), 0, 0)$, is extracted from the steady state numerical simulation at the injection axial position, and reported in Fig. 5.1.

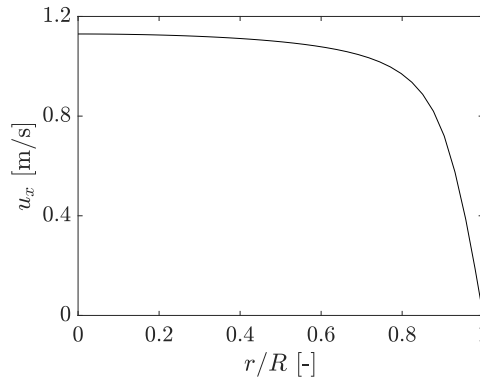


Fig. 5.1 Velocity profile extracted from simulations at the injection axial position.

Figure 5.2 reports the results obtained by applying the two formulations of the transfer function, \hat{H} and $\hat{H}_{area-averaged}$, to the LITGS time signal at the first axial location (x_1). This means that the time trace x_1 (after performing a moving-average smoothing with span equal to 10) is transported by the model implementing the shear dispersion. The model output (computed numerically in Matlab) shows an encouraging agreement with experimental results: convective times, decrease in peaks and signals shape are globally well predicted, especially for the argon and carbon dioxide cases. The helium case shows a more relevant mismatch in terms of signal shape: this is mainly due to first trace (used as input to the model), which is affected by the radial impingement and by more relevant noise. In every case, the area average formulation shows a worse agreement with LITGS combined with increased dispersion: this is expected, since the same effect has been detected in CFD results discussed in §4.7.

It should be noted that using the first LITGS trace as boundary condition for the model is necessary to test if the assumption of neglecting the diffusion is realistic in this framework, and to verify that the shear dispersion theory is sufficient to explain the advection of the compositional spot. Further, the present one-dimensional formulation would not be capable of predicting more complex phenomena, such as the generation of the wave itself after the radial injection.

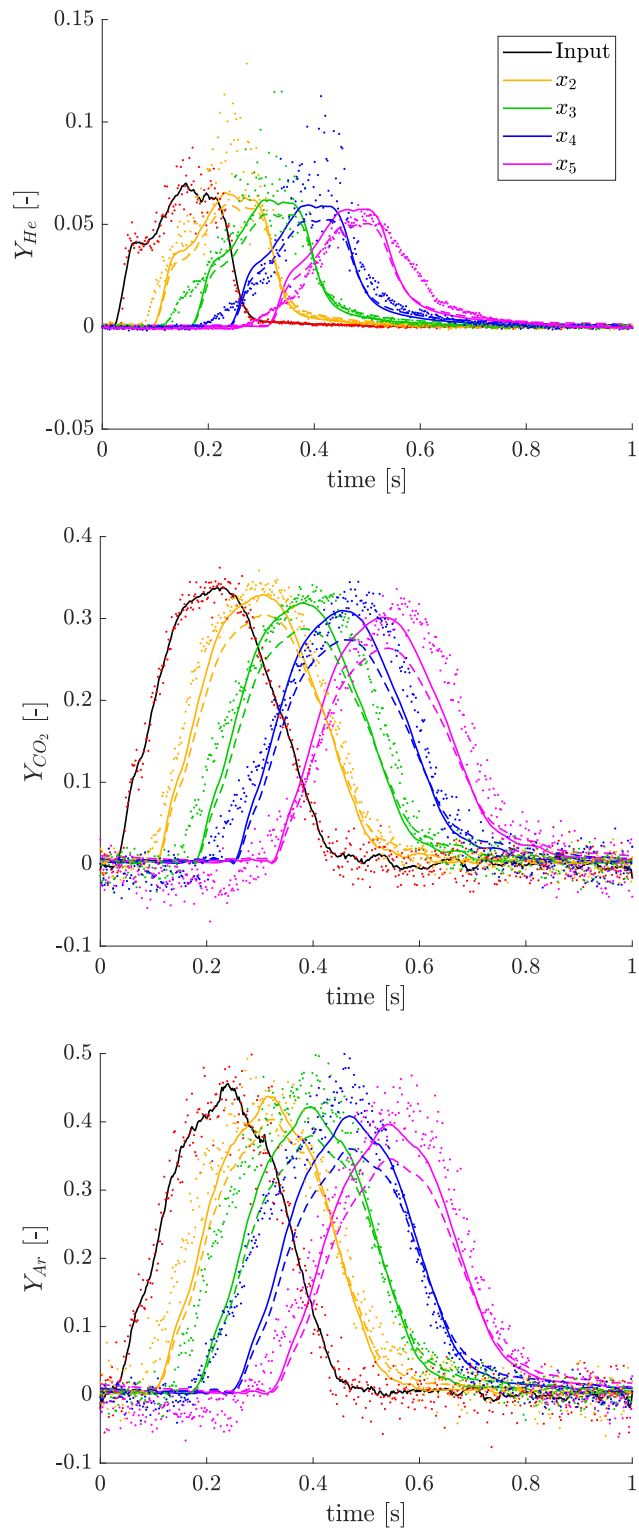


Fig. 5.2 Compositional wave prediction by the one-dimensional model and comparison with LITGS (dots). Mass flow averaged (solid lines) and area averaged formulation (dashed lines). The first LITGS time trace is smoothed and used as input for the model.

5.3 Model sensitivity to the velocity profile

In this section, the wave advection predicted by the mass flow averaged formulation of the model is studied assuming different main flow conditions, i.e. velocity profiles $u_x(r)$. The values summarized below are not correlated to specific experimental test cases, since the present investigation is simply meant to assess the influence of arbitrary velocity profiles.

- velocity profile used in the previous section (extracted from steady state simulations and plotted in Fig. 5.1);
- fully developed laminar profile having $u_{bulk} = 0.7$ m/s ($Re_D \approx 1960$) and parabolic distribution over radius, according to

$$u_x(r) = 2u_{bulk} \left(1 - r^2/R^2\right)$$

- fully developed turbulent profile having $u_{bulk} = 4$ m/s ($Re_D \approx 11210$) and the following distribution over radius:

$$u_x(r) = Cu_{bulk} \left(1 - r/R\right)^{1/n}$$

where $n = 5$ and C is a factor only dependent on n , ensuring consistency of maximum and bulk values of the profile;

- fully developed turbulent profile having $u_{bulk} = 4$ m/s and the same radial distribution defined before, but assuming $n = 7$.

Results referred to the argon case are reported in Fig. 5.3, where the argon mass fraction is represented in the space-time domain (axial position normalized by the downstream length). The boundary condition used for the model is always the first LITGS time trace (as previously described). It can be noticed that the parabolic velocity profile causes a much more relevant influence of the differential convection on the traveling wave if compared to the case investigated with CFD and experiments. Differences in terms of wave convection are not much significant, since the bulk velocity is only slightly lower.

The implementation of turbulent velocity profiles results in an obviously faster convection of the wave, while no relevant influence of the profile shape is observed on the wave dispersion: this is consistent with observations made by Giusti *et al.* [20] on their “entropy transfer function”, which also took into account only the Taylor dispersion mechanism.

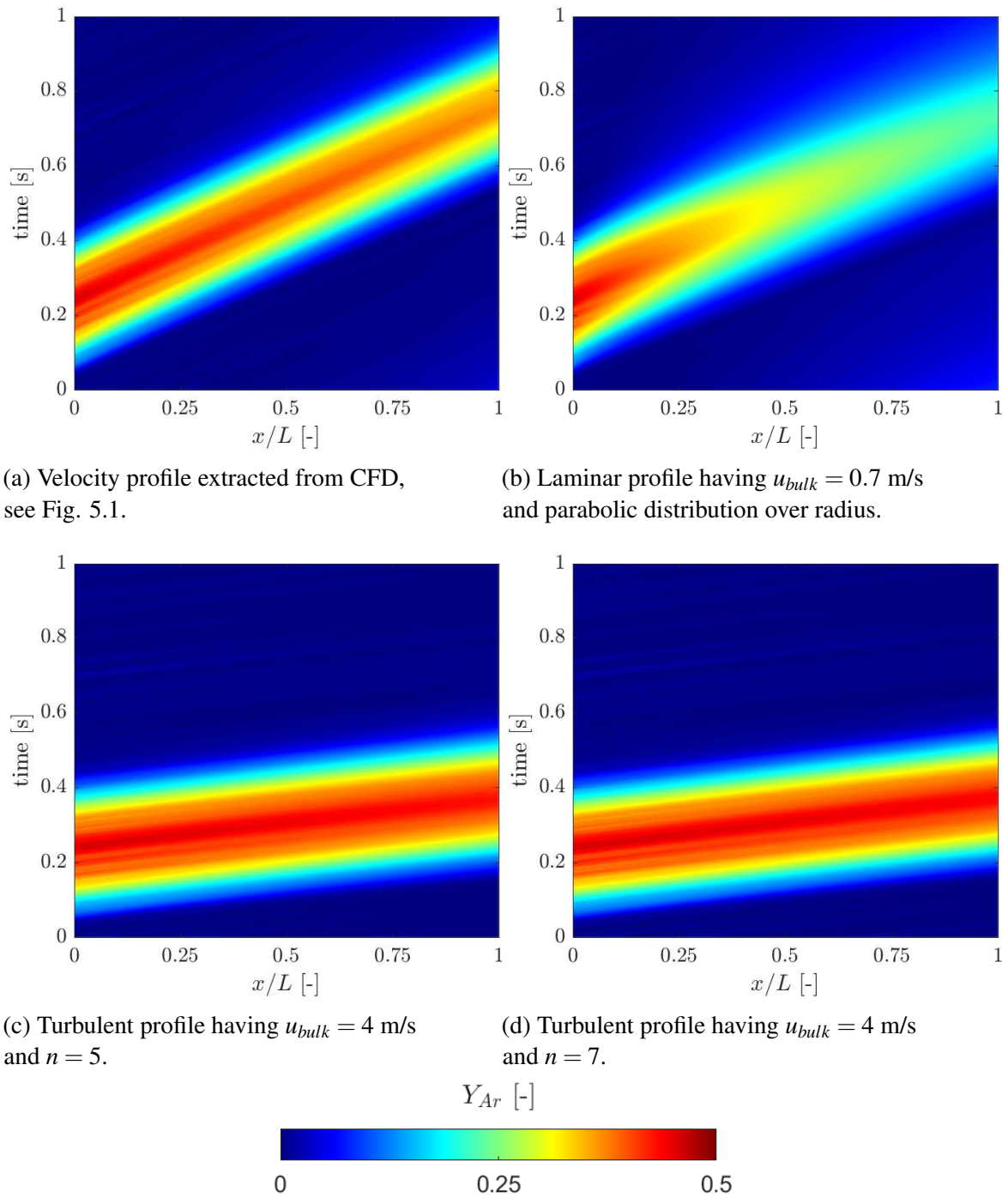


Fig. 5.3 Argon compositional wave predicted by the model in the investigated configuration, for different convective velocity profiles.

Chapter 6

Conclusions and future work

The Laser Induced Thermal Grating Spectroscopy (LITGS) technique has been successfully applied to detect and time resolve small unsteady composition variations in a non-reacting ducted flow of air, in which secondary gas flows of helium, carbon dioxide and argon are pulsed. High frequency (500 Hz) measurements have been performed using a low energy PIV laser to generate the grating, and signal standard deviations of the order of 2% are achieved for the Ar and CO₂ cases. More noise is present in the helium case because of its higher thermal quenching, which rises difficulties in capturing its LITGS signal.

Experiments also highlighted some disadvantages of the technique. The main complication is the necessity of an absorber species at the laser wavelength to generate the grating: biacetyl was used in the employed set-up, and its presence produces changes in the mean flow properties that are taken into account. The consumption rate of biacetyl is also the main factor limiting the main mass flow, since a sufficient quantity of seeder is always necessary to produce the LITGS signal. A second problem is the trade off between intrusiveness caused by thermalisation and spatial resolution: in fact, a small probe volume is desirable to avoid averaging effects, but a larger one allows longer residence times and reduces the flow temperature increase. Further, the higher noise in the helium case could be reduced increasing the pump laser pulse to obtain more defined LITGS signals, with obvious consequences on intrusiveness. Measurements performed should allow the quantification of the strength and amplitude of the composition wave approaching a flow discontinuity (such as nozzles, orifices, or NGVs) and help to analyze the indirect noise generated from their acceleration.

A CFD procedure has been developed from zero in the OpenFOAM framework to simulate the same experimental conditions, in order to assess the reliability of the solver *reactingFoam* in predicting transient compositional spots. Results of unsteady RANS simulations showed an encouraging agreement for the argon and carbon dioxide cases. The helium simulation highlighted the need for a more articulate transient boundary condition for the injection

if compared to the employed one, which is derived a posteriori from the experiments. It has been verified that modifications of the laminar and turbulent Schmidt numbers do not produce changes in the compositional wave dispersion. This suggests that (in the investigated cases) the diffusion of the spot is governed by shear dispersion, and that a more complex diffusion model would unlikely produce better results. Further, the sensitivity study to the probing method in simulations demonstrated that the estimated grating size is not significantly affecting the LITGS measurements in the employed set-up; this confirms the possibility to use the experimental results as a starting point for one-dimensional analytical models of compositional waves dispersion. A recommended further step on the numerical side is the employment of the compressible solver *reactingFoam* for indirect noise simulations. Obviously, the reduction of the time step, necessary to have good frequency resolution, and the long periods that needs to be simulated to separate direct and indirect contributors are going to require much higher computational resources.

Finally, a theoretical model of the advection of compositional waves has been proposed and compared to experimental results. The presented one-dimensional theory takes into account only the shear dispersion mechanism arising from spatial variations of the convective velocity profile. Results provided by the model showed a good agreement with LITGS traces, proving that the diffusion of the compositional wave (in the present configuration) is governed by Taylor dispersion. The proposed model is suitable to improve accuracy of low-order acoustic network codes, simply requiring an estimation of the convective velocity profile and the initial shape of the wave.

References

- [1] Aerospace and Defence Industries Association for Europe (2010). ACARE 2010 Final Report. <http://www.acare4europe.org/documents/final-report>.
- [2] Aerospace and Defence Industries Association for Europe (2011). ACARE Flightpath 2050 - Program summary. <http://www.acare4europe.org/sria/flightpath-2050-goals>.
- [3] ANSYS (2006). Modeling Turbulent Flows. *Introductory FLUENT Training*.
- [4] ANSYS (2013). Species Transport Equations. *Introductory FLUENT Training*.
- [5] Bake, F., Richter, C., Mühlbauer, B., Kings, N., Röhle, I., Thiele, F., and Noll, B. (2009). The Entropy Wave Generator (EWG): A reference case on entropy noise. *Journal of Sound and Vibration*, 326(3-5):574–598.
- [6] Bakker, A. (2008). Dartmouth College - Computational Fluid Dynamics course material. <http://www.bakker.org/dartmouth06/engs150/>.
- [7] Baldwin, B. and Barth, T. J. (1990). A one-equation turbulence transport model for high Reynolds number wall-bounded flows. *29th Aerospace Sciences Meeting, Ames Research Center, Moffett Field, CA*.
- [8] Cambridge HPC (2017). Darwin Cluster webpage. <http://web.archive.org/web/20080207010024/http://www.808multimedia.com/winnt/kernel.htm>.
- [9] Cravero, C. (2016). University of Genova - Computational Fluid Dynamics - Lecture notes.
- [10] Cummings, E. B., Leyva, I. A., and Hornung, H. G. (1955). Laser-induced thermal acoustics (LITA) signals from finite beams. *Applied Optics*, 34(18):3290–3302.
- [11] De Domenico, F., Rolland, E. O., and Hochgreb, S. (2017). Detection of direct and indirect noise generated by synthetic hot spots in a duct. *Journal of Sound and Vibration*, 394:220–236.
- [12] De Domenico, F., Shah, P., Williams, B. A., Ewart, P., Lowe, M. S., Fan, L., and Hochgreb, S. (2018). High Frequency Measurement of Temperature and Composition Spots with LITGS. In *Proceedings of the ASME 2018 Turbomachinery Technical Conference & Exposition*.
- [13] Dowling, A. P. and Mahmoudi, Y. (2015). Combustion noise. *Proceedings of the Combustion Institute*, 35(1):65–100.

- [14] Durán I., Moreau S., P. T. (2013). Analytical and Numerical Study of Combustion Noise Through a Subsonic Nozzle. *AIAA Journal*, 51(1).
- [15] Eckstein, J. (2004). *On the Mechanisms of Combustion Driven Low-Frequency Oscillations in Aero-Engines*. PhD thesis, TU Munchen.
- [16] Eggels, J. G. M., Unger, F., Weiss, M. H., Westerweel, J., Adrian, R. J., Friedrich, R., and Nieuwstadt, F. T. M. (1994). Fully developed turbulent pipe flow: a comparison between direct numerical simulation and experiment. *Journal of Fluid Mechanics*, 268(1):175–210.
- [17] Fick, A. (1855). Ueber Diffusion. *Annalen der Physik*, 170(1):59–86.
- [18] Filippone, A. (2014). Aircraft noise prediction. *Progress in Aerospace Sciences*, 68:27–63.
- [19] Gaetani, P., Persico, G., and Spinelli, A. (2015). Entropy Wave Generator for Indirect Combustion Noise Experiments in a High - Pressure Turbine. *11th European Conference on Turbomachinery Fluid dynamics & Thermodynamics*, pages 1–13.
- [20] Giusti, A., Worth, N. A., Mastorakos, E., and Dowling, A. P. (2017). Experimental and Numerical Investigation into the Propagation of Entropy Waves. *AIAA Journal*, 55(2):446–458.
- [21] Greenshields, C. J. (2015). Openfoam 3.0.1 user guide. *OpenFOAM Foundation Ltd*.
- [22] Hake, M. I. (2014). Experimental Design to Determine the Effect of Temperature and Mach Number on Entropy Noise. *B.Sc. Thesis - Massachusetts Institute of Technology*.
- [23] Holmén, V. (2012). Methods for vortex identification. *M.Sc. Thesis - Lund University*.
- [24] Holzmann, T. (2016). Mathematics, Numerics, Derivations and OpenFOAM®. *Holzmann CFD*.
- [25] ICAO (2010). Environmental Report - Aviation ad climate change.
- [26] Ihme, M. (2017). Combustion and Engine-Core Noise. *Annual Review of Fluid Mechanics*, 49(1):277–310.
- [27] Launder, B. E. and Spalding, D. B. (1974). The Numerical Computation of Turbulent Flows. *Computer Methods in Applied Mechanics and Engineering*, 3(2):269–275.
- [28] Lourier, J.-M., Huber, A., Noll, B., and Aigner, M. (2014). Numerical Analysis of Indirect Combustion Noise Generation Within a Subsonic Nozzle. *AIAA Journal*, 52(10):2114–2126.
- [29] Magri, L. (2017). On indirect noise in multicomponent nozzle flows. *Journal of Fluid Mechanics*, 828:R2.
- [30] Magri, L., O’Brien, J., and Ihme, M. (2016). Compositional inhomogeneities as a source of indirect combustion noise. *Journal of Fluid Mechanics*, 799(2016):1–11.

- [31] Marble, F. E. and Candel, S. M. (1977). Acoustic disturbance from gas non-uniformities convected through a nozzle. *Journal of Sound and Vibration*, 55(2):225–243.
- [32] Menter, F. (1993). Zonal two equation $k-\omega$ turbulence models for aerodynamic flows. In *23rd Fluid Dynamics, Plasmadynamics, and Lasers Conference*, page 2906.
- [33] Menter, F. (1994). Two-equation eddy-viscosity turbulence models for engineering applications. *AIAA Journal*, 32(8):1598–1605.
- [34] Morgans, A. S., Goh, C. S., and Dahan, J. A. (2013). The dissipation and shear dispersion of entropy waves in combustor thermoacoustics. *Journal of Fluid Mechanics*, 733.
- [35] Mühlbauer, B., Noll, B., and Aigner, M. (2009). Numerical Investigation of the Fundamental Mechanism for Entropy Noise Generation in Aero-Engines. *Acta Acustica United with Acustica*, 95:470–478.
- [36] Patel, V. C., Rodi, W., and Scheuerer, G. (1985). Turbulence models for near-wall and low Reynolds number flows - A review. *AIAA Journal*, 23(9):1308–1319.
- [37] Peters, N. (2000). *Turbulent Combustion*. Cambridge University Press, Cambridge.
- [38] Rodrigues, J. (2017). On entropy-generated acoustics in compressible flows. *First Year PhD Report - University of Cambridge*.
- [39] Rodrigues, J., Rolland, E. O., De Domenico, F., and Hochgreb, S. (2017). Computational Investigation of Direct Noise Generated by Synthetic Hot Spots in a Duct. *24th International Congress on Sound and Vibration*, pages 1–8.
- [40] Rolland, E. O., De Domenico, F., and Hochgreb, S. (2017a). Direct and Indirect Noise Generated by Injected Entropic and Compositional Inhomogeneities. In *Proceedings of ASME Turbo Expo 2017: Turbomachinery Technical Conference and Exposition*, pages 1–13.
- [41] Rolland, E. O., De Domenico, F., and Hochgreb, S. (2017b). Theory and application of reverberated direct and indirect noise. *Journal of Fluid Mechanics*, 819:435–464.
- [42] Rolls-Royce (1996). *The jet engine*. Rolls-Royce plc, Derby, England.
- [43] Rumsey, C. (2017). Turbulence Modeling Resource: the Menter Shear Stress Transport Turbulence Model. <https://turbmodels.larc.nasa.gov/sst.html>.
- [44] Sattelmayer, T. (2003). Influence of the Combustor Aerodynamics on Combustion Instabilities From Equivalence Ratio Fluctuations. *Journal of Engineering for Gas Turbines and Power*, 125(1):11.
- [45] Schlichting, H. (1979). *Boundary-Layer Theory*. McGraw-Hill, Braunschweig, Germany.
- [46] Smagorinsky, J. (1963). General Circulation Experiments With the Primitive Equations. *Monthly Weather Review*, 91(3):99–164.

-
- [47] The Engineering Toolbox (2018). Air and gases properties. <https://www.engineeringtoolbox.com/>.
- [48] Tominaga, Y. and Stathopoulos, T. (2007). Turbulent Schmidt numbers for CFD analysis with various types of flowfield. *Atmospheric Environment*, 41(37):8091–8099.
- [49] Ubaldi, M. (2017). University of Genova - Combustion - Lecture notes.
- [50] Versteeg, H. K. and Malalasekera, W. (1995). *An Introduction to Computational Fluid Dynamics - The Finite Volume Method*. New York, first edition.
- [51] Wilcox, D. (1988). Reassessment of the scale-determining equation for advanced turbulence models. *AIAA Journal*, 26(11):1299–1310.
- [52] Williams, B., Wijeyasinghe, N., Guan, X., and Ewart, P. (2012). Laser Induced Grating Spectroscopy for multi-parameter combustion diagnostics. University of Oxford - internal presentation.
- [53] Williams, G. (1985). *Combustion Theory*. Addison-Wesley, York.
- [54] Wolfram (2017). Wolfram CDF Player. <https://www.wolfram.com/cdf-player/>.
- [55] Xia, Y., Duran, I., Morgans, A. S., and Han, X. (2016). Dispersion of Entropy Waves Advecting through Combustor Chambers. *23rd International Congress on Sound and Vibration*.

Appendix A

Numerical Setup

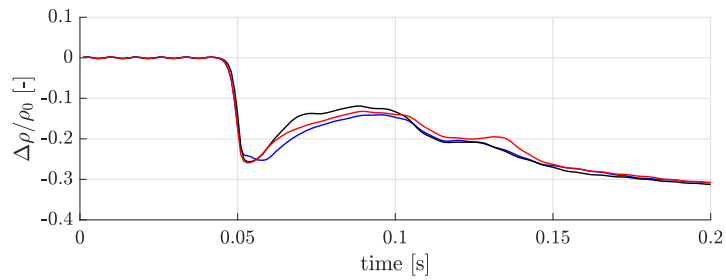
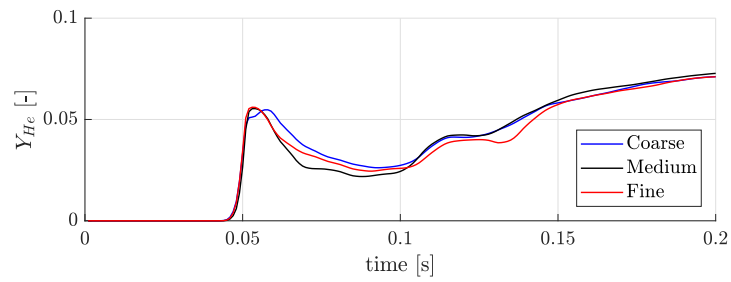
A.1 Mesh convergence study

A grid independence study was performed on the geometry used to simulate the injection, after removing the inlet part of the domain (as described in §4.4). Signals from the first probe (x_1) placed 13 cm downstream of the injection are compared in terms of mass fraction, Y_{He} , and normalized density gradient $\Delta\rho/\rho_0$ (where ρ_0 is the base flow steady state density). The study refers only to the injection period (0.2 seconds) and to the helium case, since this is where the highest density gradients are expected and also where the smallest absolute values of mass fraction needs to be captured.

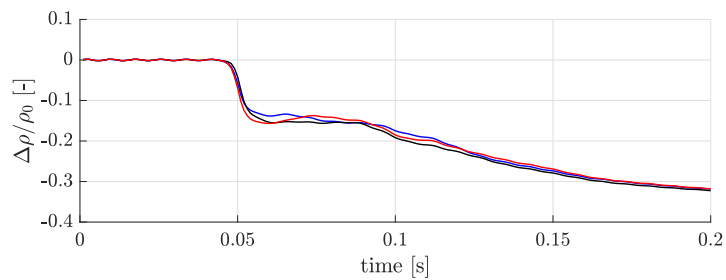
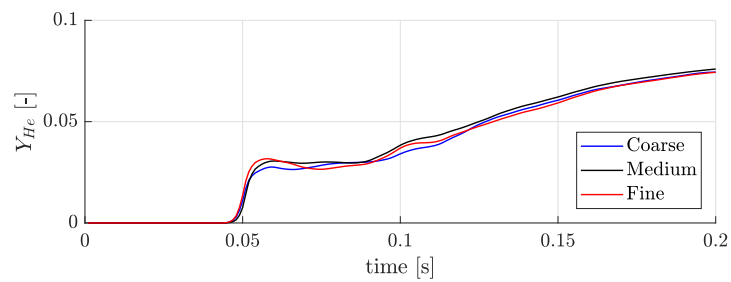
Table A.1 Mesh convergence study: comparison between the three tested grids.

	Number of cells	Computational time [hours]
Coarse	~435k	~3.3
Medium	~711k	~8.6
Fine	~862k	~11.1

Every case was run employing 32 cores on the University of Cambridge’s High Performance Computing system (Darwin cluster) [8]. The “medium” mesh is employed, having been considered the best compromise between spatial resolution and computational time. In fact, Figures A.1a and A.1b show that small and localized differences appears only when the punctual signal is considered, and those do not modify the overall trend or the phenomena characteristic times. Mean values over the radius orthogonal to the injection at the same axial location show a even better agreement, meaning that the convection-diffusion process is captured fairly well even with the coarse mesh.



(a) Punctual probe.



(b) Average over radius.

Fig. A.1 Mesh convergence study, helium case, injection period only. (a): Signal of a punctual probe on the center line, 13 cm downstream of the injection. Helium mass fraction (top) and normalized density variation (bottom). (b): Signals averaged over radius at the same axial location.

A.2 Numerical schemes

```

/*----- C++ -----*/
=====
\ \ \ \ \ Field      | OpenFOAM: The Open Source CFD Toolbox
\ \ \ \ \ Operation  | Version: 4.x
\ \ \ \ \ And        | Web: www.OpenFOAM.org
\ \ \ \ \ Manipulation
/*-----*/
FoamFile
{
  version      2.0;
  format       ascii;
  class        dictionary;
  location     "system";
  object       fvSchemes;
}
// ***** //

ddtSchemes
{
  default      steadyState;
}

gradSchemes
{
  default      cellLimited Gauss linear 1;
}

divSchemes
{
  default      none;

  div(phi,U)   bounded Gauss upwind;

  div(phi,e)   bounded Gauss upwind;
  div(phi,Ekp) bounded Gauss upwind;

  div(phi,omega) bounded Gauss upwind;
  div(phi,k)   bounded Gauss upwind;

  div(((rho*nuEff)*dev2(T(grad(U)))) Gauss linear;
}

laplacianSchemes
{
  default      Gauss linear corrected;
}

interpolationSchemes
{
  default      linear;
}

snGradSchemes
{
  default      corrected;
}

wallDist
{
  method meshWave;
}

// ***** //

```

Fig. A.2 Numerical schemes used in OpenFOAM for the steady simulations (*rhoSimpleFoam*).

First order numerical schemes have been employed for the steady simulations in order to ensure the stability of the code, especially for a future use with higher main flow mass flow rates. Further, the steady state solution of the simplified geometry has no gradients that need to be captured, and it is computed only to provide a more accurate initial condition of the steady flow field before the transient injection.

```

/*-----* C++ */
=====
\ \ \ \ \ F i e l d      | OpenFOAM: The Open Source CFD Toolbox
\ \ \ \ \ O p e r a t i o n | Version: 4.x
\ \ \ \ \ A n d             | Web: www.OpenFOAM.org
\ \ \ \ \ M a n i p u l a t i o n |
/*-----*/
FoamFile
{
    version      2.0;
    format       ascii;
    class        dictionary;
    location     "system";
    object       fvSchemes;
}
// ***** //

ddtSchemes
{
    default      Euler;
}

gradSchemes
{
    default      cellLimited Gauss linear 1;
}

divSchemes
{
    default      none;

    div(phi,U)   Gauss linearUpwind default;
    div(phi,Yi_h) Gauss limitedLinear 1;
    div(phi,K)   Gauss limitedLinear 1;
    div(phiid,p) Gauss limitedLinear 1;
    div(phi,omega) Gauss upwind;
    div(phi,k)   Gauss upwind;
    div(((rho*nuEff)*dev2(T(grad(U)))) Gauss linear;
}

laplacianSchemes
{
    default      Gauss linear corrected;
}

interpolationSchemes
{
    default      linear;
}

snGradSchemes
{
    default      corrected;
}

wallDist
{
    method meshWave;
}

// ***** //

```

Fig. A.3 Numerical schemes used in OpenFOAM for the unsteady simulations (standard and modified *reactingFoam*).

Second order schemes are used in the unsteady simulations for each spatial derivative except for the turbulence quantities, in order to ensure stability. Implicit Euler scheme is employed for time derivatives.